

Full length article

Constitutive description of skin dermis: Through analytical continuum and coarse-grained approaches for multi-scale understanding

Andrei Pissarenko^a, Carlos J. Ruestes^b, Marc A. Meyers^{a,*}

^aUniversity of California, San Diego, CA, United States

^bInstituto Interdisciplinario de Ciencias Básicas, Facultad de Ciencias Exactas y Naturales, Universidad Nacional de Cuyo, CONICET, Mendoza, Argentina

ARTICLE INFO

Article history:

Received 4 November 2019

Revised 1 January 2020

Accepted 20 January 2020

Available online 31 January 2020

Keywords:

Skin

Collagen

Coarse grain modeling

Molecular dynamics

Constitutive modeling

ABSTRACT

Although there are many successful descriptions of the mechanical response of dermis at different levels of complexity and incorporating varying degrees of the physical phenomena involved in deformation, observations indicate that the unraveling of fibers involves a complex three-dimensional process in which they interact in ways that resemble a braided pattern. Here we develop two complementary treatments to gain a better understanding of the mechanical response of dermis: a) an analytical treatment incorporating fibril stiffness, interfibrillar frictional sliding, and the effect of lateral fibers on the extension of a primary fiber; b) a coarse-grained molecular dynamics model comprised of an array of parallel curved fibrils simulating a fiber. Interfibrillar frictional sliding and stiffness are also captured. Both analytical and molecular dynamics models operate at a scale compatible with the wavelength of collagen fibers (~10 μm). The constitutive description presented here incorporates important physical processes taking place during deformation of dermis and thus represents an advance in our understanding of these phenomena.

Statement of Significance

Microstructural observations of the dermis of skin during tensile deformation indicate that the unraveling of fibers involves a complex three-dimensional process which replicates the effects of braiding. Two complementary constitutive modeling treatments were developed to gain a better understanding of the mechanical response of dermis: an analytical treatment incorporating fibril stiffness, interfibrillar sliding, and the effect of transverse fibers; and a coarse-grained molecular dynamics model describing the fibril bundling effect.

An important novel aspect of the current contribution is the recognition that tridimensional collagen fiber arrangements play an important role in the mechanical response. The constitutive description presented here incorporates physical processes taking place during deformation of the dermis and thus represents an advance in our understanding of these phenomena.

© 2020 Acta Materialia Inc. Published by Elsevier Ltd. All rights reserved.

1. Introduction: constitutive modeling of skin

Skin is the outer layer of living organisms and is, by some measures, the largest organ of vertebrates. It performs a number of essential functions for the survival of organisms, such as protection, temperature and moisture regulation, in addition to sensory functions. Constitutive modeling is essential in representing the physical behavior of materials, and accordingly enables their

characterization, classification, and comparison. The selection of an appropriate formulation that accurately and consistently tracks the mechanical behavior of a given material is therefore of fundamental importance. For a soft tissue like skin, with anisotropy, non-linear elasticity, viscoelasticity, and dissipative behavior, this choice can become complex, and as a result a variety of models have been proposed and compared [1–5]. The physical parameters of a model can be used to identify processes occurring in the microstructure; they can help differentiating between healthy and diseased tissue, or generate ideas for applications for example

* Corresponding author.

E-mail address: mameyers@ucsd.edu (M.A. Meyers).

in biomimicry with synthetic grafts, wearable sensors, and dermal armors.

The constitutive models that have been developed to describe the mechanical response of skin can be roughly classified into three classes:

- (a) Phenomenological models, which are essentially mathematical descriptions lacking any physical insight. Examples are the Ogden [6] and Mooney-Rivlin [7,8] models which were originally developed for elastomers and found use in skin. The principal advantage is their simplicity and ease-of-use. However, their inability to capture tissue anisotropy limits their interest. Viscoelasticity and the dissipative behavior of skin can also be described by the Quasi-Linear Viscoelastic theory [9], differential viscoelasticity [10], or the Volokh model [11].
- (b) Semi-structural models. These formulations take into account the contribution of the main constituents of skin (i.e. collagen, elastin, ground substance), their relative mechanical properties and their structural arrangement. Anisotropy can be included by introducing preferred directions. A prominent example is the Arruda-Boyce eight-chain [12,13] model for non-linear elasticity, and the Bergstrom-Boyce [14] model which includes viscoelasticity. Extended rheological models from Generalized Maxwell models can be found as well [15,16].
- (c) Semi-structural models with dispersed fibers [17]. The orientation and crimp of collagen and elastin fibers are described by distribution functions, represented either in a discrete fashion [18], or with some degree of fiber dispersion, incorporated by angular integration [19,20] or using generalized structure tensors [21]. Interactions between components can also be taken into account, with for example interfibrillar shear [22–24]. Consequently, there tends to be a larger number of parameters to identify, but the mechanisms occurring in the microstructure are better represented. It is important to note that for each constituent, a phenomenological representation is usually chosen.

Structurally-based models require prior knowledge of the structural arrangement within the tissue, which can be quite complex in the context of skin. Thus, their constitutive parameters have not yet been completely defined and quantified.

2. Structure of the dermis and deformation process

There are three principal layers in skin: hypodermis, dermis, and epidermis on the outermost side. The in-plane tensile properties of skin are to a large extent dictated by the dermis [25], the principal structural component of skin, as it is often assumed in several constitutive models of skin [20,22,26]. This is particularly relevant for models that emphasize on the effects of the microstructure of the collagenous network in the dermis. Other composite models that account for the contribution of the distinctive layers of skin [27–29] generally focus on deformation modes involving through-plane deformation, or are associated with experimental studies where the skin is directly tested from the outer surface, such as in vivo conditions [30]. Such models also often use simpler constitutive laws for each layer, to reduce complexity. The stratum corneum, which is the highly keratinized outermost layer of the epidermis, serves as a first protection against the environment, and although it is generally stiffer than the dermis layers [27], it is much thinner than the reticular dermis and has a much lower maximum tensile stress, around 1 MPa, with a maximum of 4 MPa [31].

The dermis is comprised of a dense network of curved collagen fibers (~70% of dry weight [2,32], or 30% volume ratio [33–35] in

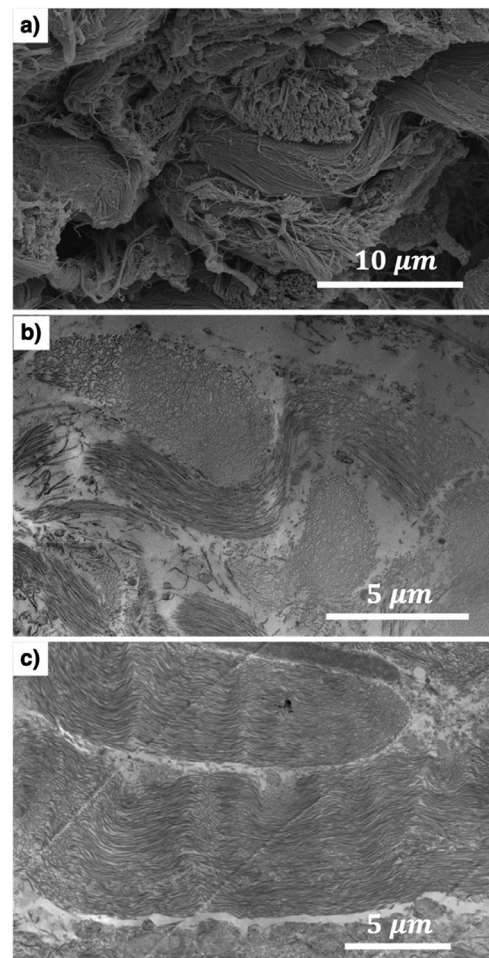


Fig. 1. (a) Scanning electron micrograph (SEM) of a longitudinal cross-section of pig dermis showing a highly entangled network of wavy collagen fibers, formed by bundles of collagen fibrils. Unpublished result, taken from the same series of SEM images that were printed in [25], and acquired following the same methods. (b) Transmission electron micrograph (TEM) of a section parallel to the dermis surface, showing similarities in entanglement and fiber crimp. (c) Post-failure TEM of a similar section of porcine dermis, after a skin sample has been deformed under uniaxial tension. The tensile direction is aligned with the horizontal axis of the image. In this state, collagen fibers have straightened and are more aligned with the tensile direction. TEM images are adapted from [25]. (For interpretation of the references to colour in this figure legend, the reader is referred to the web version of this article.)

the hydrated state) with diameters ranging 2–10 μm [16,25]. These are formed by dense bundles of parallel fibrils (~50–120 nm in diameter [25]). These fibers are embedded in a viscoelastic matrix often called the “ground substance”, and a transverse network of elastin fibers, comprising 1–4% of the dry weight [2] (or 2–10% of the volume ratio [33–35]) of the dermis. Additionally, two sublayers of the dermis can be distinguished, with the papillary dermis lying underneath the epidermis layer, followed by the reticular dermis right below. From a microstructural standpoint, the papillary dermis is usually much thinner, and collagen fibers in this layer are finer and more densely distributed than for the reticular dermis, with a prominence of elastic fibers oriented perpendicular to the surface of the epidermis to maximize cohesion with the overlying layer [1,36]. Nonetheless, significantly more quantitative information is available on the fibrous networks in the thicker reticular dermis [2,25,33], to which the strength and the extensibility properties of skin are often conferred.

Fig. 1 shows a scanning electron micrograph (SEM) and transmission electron micrographs (TEM) of a longitudinal cross-section of untested pig reticular dermis for the SEM image (i.e. along the

Langer lines, Fig. 1a) and surface sections of the reticular dermis of pig skin for the TEM images (i.e. parallel to the surface of the skin), taken before testing (Fig. 1b) and after application of a uniaxial tensile load until sample failure (Fig. 1c). These images are reproduced from the series of micrographs that were acquired for publication in [25], where the preparation methods are described. The fibers can be clearly seen and the bundles of fibrils that compose them show a characteristic D-banding in the transmission electron micrograph, which is caused by the 67 nm band pattern of collagen. The collagen fibers have, for pig skin, a wavelength of $\sim 10 \mu\text{m}$ [25] in the resting state. As the skin is stretched in tension, the structure undergoes a number of changes, which were classified by Yang et al. [37] into rotation, straightening, inter-fiber and intra-fiber sliding, followed by fracture, resulting in highly aligned, straight collagen fibers, as Fig. 1c shows. There is some residual waviness, with a much smaller wavelength, that is attributed to the spring-back of the collagen fibrils after unloading caused by stress gradients. Thus, the non-linear elasticity of skin, and generally of soft collagenous tissues, can be attributed to two concurrent mechanical processes:

- The alignment of the loaded collagen fibers in the principal direction of tension by rotation.
- The straightening of the curved collagen fibers, which is marked by the transition from a tensile behavior mainly dictated by the bending stiffness of the fibers to a behavior imposed by their tensile stiffness, which is in general at least an order of magnitude higher for slender structures.

Several structurally-based formulations have attempted to represent fiber crimp by introducing rigid corners, sinusoidal, helical, and more recently semi-circular descriptions of collagen fiber geometry, as reviewed by Sherman et al. [38]. The semi-circular, or horseshoe patterns were introduced by Sherman et al. [16] and by Ma et al. [39] independently, but were resolved using different approaches. A considerable advantage of this description is that it follows quite well the observed curvature of collagen fibers in the dermis with a reduced number of descriptive parameters, assuming that the fiber is confined in a plane.

Another important feature of the arrangement of collagen is the tridimensional nature of the organization of fibers. It is well known that, in planes parallel to the outer surface of the skin, collagen fibers follow preferred orientations, defined by the so-called Langer lines. These correspond to directions of pre-existing tension in the tissue, which directly affect the anisotropy of the material. Ni An-naidh et al. [40] reported that the orientation of collagen fibers in the dermis of human skin follows a bimodal distribution. Jor et al. [41] measured orientations of collagen fibers in the thickness (out-of-plane) direction of the dermis of porcine skin, with different cross-sectional angles, taken with respect to the axis of the spine. Interestingly, they also find a bimodal distribution of orientations (centered around the out-of-plane axis), with principal angles and standard deviations that vary according to cross-section and location on the body. Such fiber distributions, in planes that are perpendicular to each other, are in direct contradiction with a layered model, where collagen fibers would be confined to parallel planes.

Only a few representations of the structure of the dermis can follow this type of arrangement. The Gasser-Ogden-Holzapfel (GOH) model [21] has been widely used for skin [40,42,43] as well as other soft collagenous tissues, and accounts for tridimensional fiber dispersion (planar dispersion is also possible assuming the fibers are confined in plane). However, in such a model, fibers deform independently, interactions are neglected, and the focal point of each fiber family does not play any physical role.

Another example of a model including a tridimensional arrangement is the orthotropic eight-chain model that was used by Kuhl et al. [13] and by Bischoff et al. [15] to simulate ten-

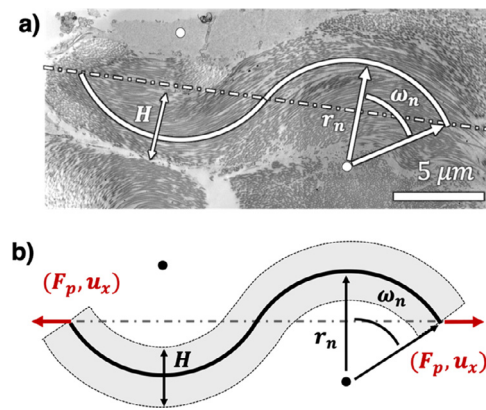


Fig. 2. One dimensional S-shaped model of wavy collagen fibers. (a) Transmission electron micrograph of a section of pig dermis parallel to the skin surface, reproduced from [25], showing that the neutral axis of a wavy collagen fiber of thickness H can be approximated by semi-circular segments with radius of curvature r_n and opening angle ω_n . (b) One-dimensional approximation of the loading configuration, where a tensile load F_p (or reciprocally a displacement u_x) is applied along the principal axis of the fiber.

sile tests on rabbit skin that were reported earlier by Lanir and Fung [44]. However, distribution in angular orientation of collagen fibers in these models is reduced to two pairs of angles, symmetric about the directions of local orthotropy. Moreover, the worm-like chain model that was used to describe fiber deformation is purely phenomenological, meaning that the constitutive parameters cannot be associated with intrinsic properties of collagen fibers.

The results of SEM, TEM, and second harmonic generation imaging (SHG) [25] indicate that a certain degree of fiber entanglement or braiding should be considered in the deformation process, adding resistive forces and a dissipative component. Pissarenko et al. [25] proposed a model experiment conducted on a triple hair braid. This experiment is also reproduced in SI I, Figure SI I showing the deformation process of the braid and the associated stress-strain curve during a loading-unloading test. Although this model analogy is quite simple, it captures some of the important physical phenomena involved in the stretching of entangled structures, as the ones that can be encountered in the dermis. We propose here a new constitutive description incorporating the lateral constraints imposed by the neighboring fibers, as well as the inter-fibrillar shear occurring during fiber straightening. A coarse-grained molecular dynamics model of a deforming collagen fiber is also presented, providing additional insight into the interactions between fibrils and the forces at stake during this process. The complete semi-structural model describes the in-plane tensile deformation of skin, with the assumption that the dermis is the main load-bearing component of the tissue for this deformation mode. In the scope of this study, the contribution of the other layers of skin is neglected. Here, the *ex vivo* uniaxial tension experiments of porcine skin reported in [25] are used to evaluate the performance of the model.

3. Numerical methods: constitutive model and coarse-grained simulations

3.1. Structure and geometry of collagen fibers

In the reference state, collagen fibers in the dermis are wavy and follow different orientations in all three directions. Using a semi-circular approximation, as shown Fig. 2a and b, an average radius of curvature r_n^0 , opening angle ω_n^0 , and thickness of the fibers H can be obtained [25]. Fibril diameter d_f and fibril density per fiber D_f were estimated from SEM and TEM characterization of col-

Table 1

Structural features of collagen fibers and fibrils in the reticular dermis, summarized from [25], for the untested pig dermis. Mean values and standard deviation (SD) are reported. Collagen orientation corresponds to the measured direction of the neutral axis of the fibers on a given section plane, with respect to the Langer line or the direction orthogonal to the tissue plane.* Indicates that the values provided were obtained from a fit with a symmetric bimodal normal distribution.

Parameter	Mean value ± SD
Fiber radius of curvature r_n^0	6.56 μm ± 3.83 μm
Fiber opening angle ω_n^0	32.1° ± 21.11°
Fiber thickness H	2.23 μm ± 0.96 μm
Fibril density per fiber D_f	0.69 ± 0.06
Fibril diameter d_f	82 nm ± 14.36 nm
Collagen orientation/Langer line (plane // dermis surface)*	33.8° ± 25.0°
Collagen orientation/Langer line (plane ⊥ dermis surface – along Langer line)*	7.8° ± 29.4°
Collagen orientation/normal to tissue (plane ⊥ to Langer line)*	64.9° ± 19.4°

lagen in the reticular dermis, as well as the orientation of the neutral axis of the fibers with respect to the Langer lines [25]. The latter shows that fibers in this region follow a bimodal distribution, centered around the axis of the Langer line, which was also reported by Ni Annaidh et al. [40]. Similar distributions are found for the planes perpendicular to the surface, as Jor et al. [41] have shown. The average values and spread of some of these parameters are reported in Table 1. These values are used as a reference for the model-based parameter estimation implemented in this study. As mentioned above, these average values mainly apply to the fibrous network in the reticular dermis. Limited data is available for collagen in the papillary dermis, and a distinction between both layers in the model would increase the number of constitutive parameters of the model.

3.2. Representative cell of the constitutive model

Fig. 3 describes the representative element of the dermis that is used in the present constitutive framework. A semi-circular collagen fiber, formed of a bundle of parallel collagen fibrils, has a neutral axis that follows the principal direction of the cell. The cell is oriented with an angle β with respect to the loading direction where $\beta \in [-\pi/2; \pi/2]$. In this description, it is assumed that loaded fibers can freely rotate, such that the realignment process does not require any added elastic energy. The load is mostly carried by the surrounding matrix in the realignment phase. As the tensile load increases, the fiber starts to straighten. One can therefore introduce an offset stretch λ_r after which the fiber becomes eventually aligned with the loading direction, and the straightening process is initiated:

$$\lambda_r = \frac{1}{\cos\beta} \tag{1}$$

Such that:

$$\sigma(\lambda) = \begin{cases} 0 & \text{if } \lambda < \lambda_r \\ \int_1^{\lambda} E_{app}(\lambda) d\lambda & \text{if } \lambda \geq \lambda_r \end{cases} \tag{2}$$

Where $\lambda_f = 1 + \lambda - \lambda_r$ is the effective stretch of the fiber, and $E_{app}(\lambda)$ is the apparent modulus of the fiber structure, which needs to be determined as a function of the deformation state. This approach follows the resolution for semicircular beam-like fibers proposed by Sherman et al. [16] for collagen fibers.

The entanglement (or braiding) of fibers is represented here with the addition of transverse fibers, lodged in the concavities of the collagen fiber that is being pulled. This generates resisting forces, that oppose the uncrimping of collagen, thus increasing the stiffness and adding potential dissipative mechanisms. The

contact is maintained throughout the deformation, and displacement of the transverse elements is allowed. This effect is represented in the schematic sequence of Fig. 3. A simplified model of this interaction is proposed in the following sections.

3.3. 2D model of fiber bundles

For the determination of the apparent modulus of the collagen fiber structure, it is considered that the fiber is already aligned with the tensile direction, as in the configuration in Fig. 4a. Collagen fibers are represented as bundles of n_f parallel fibrils in a two-dimensional array, joined by an interstitial matrix. The neutral axis of the fiber can be approximated by a semi-circular wire, described by its initial radius of curvature r_n^0 and opening angle ω_n^0 (as described in Fig. 4b). With an applied load F_p (or an applied displacement u_x) at its extremities, the fiber straightens and unfolds, before undergoing pure tension. In order to facilitate the resolution of the stress-stretch response of the proposed model, the following hypotheses are made:

- H1 – The k -th fibril away from the neutral wire is formed by two segments with radii of curvature r_k^+ and r_k^- , such that:

$$r_k^\pm = r_n \pm k(d_f + d_{int}) \tag{3}$$

Where d_f is the cross-sectional diameter of a fibril, and d_{int} is the interspacing distance between two consecutive fibrils. Note that $d_{int} = H(1 - D_f)/(n_f - 1)$, with $n_f = [HD_f/d_f]$ the number of fibrils per fiber (and $[x]$ is the integer part of x). The radius r_k^+ describes the portion of the fibril that lies on top of the convex part of the neutral wire, and the radius r_k^- corresponds to the portion lodged in the concave part. An entire fibril is the assembly of two segments with radii r_k^+ and r_k^- , connected at the angle ω_n^0 . For the sake of simplicity, it is assumed that the distance between successive fibrils does not change during deformation.

- H2 – The matrix in the interstice between fibrils is much softer compared to the collagen fibrils. It is assumed that the shear stress τ is the only significant component of stress acting during deformation, and it is linearly related to the shear strain γ via the shear modulus G_m . Shear strain can be quantified by evaluating the relative sliding occurring between adjacent fibrils during straightening, as illustrated in Fig. 4a,b.
- H3 – During the straightening phase, the effective length of the collagen fibrils does not change. This implies that in this phase, the deformation of the fibrils is bending-dominated, in the absence of normal strain. Consequently, the effective fiber length L_f can be expressed as a product of the radius of curvature r_n and the opening angle ω_n of the neutral fibril, at any stage of the deformation before the fiber is fully straightened:

$$L_f/4 = r_n^0 \omega_n^0 = r_n^t \omega_n^t \tag{4}$$

The superscripts 0 and t denote the initial and current configurations, respectively. Consequently, for an applied displacement u , the configuration of the neutral fibril can be fully resolved if the initial configuration is known:

$$u/4 = r_n^t \sin\left(\frac{L_f}{4r_n^t}\right) - r_n^0 \sin\left(\frac{L_f}{4r_n^0}\right) \tag{5}$$

Following (H1), the configuration of the other fibrils can be determined as well.

- H4 – The deformation of the fiber is described using a piecewise function, with a distinction between the straightening phase, and the phase where the fiber is fully taut and undergoes tension. The behavior of the fiber switches from bending-dominated to purely tensile. The transition stretch λ_c can be

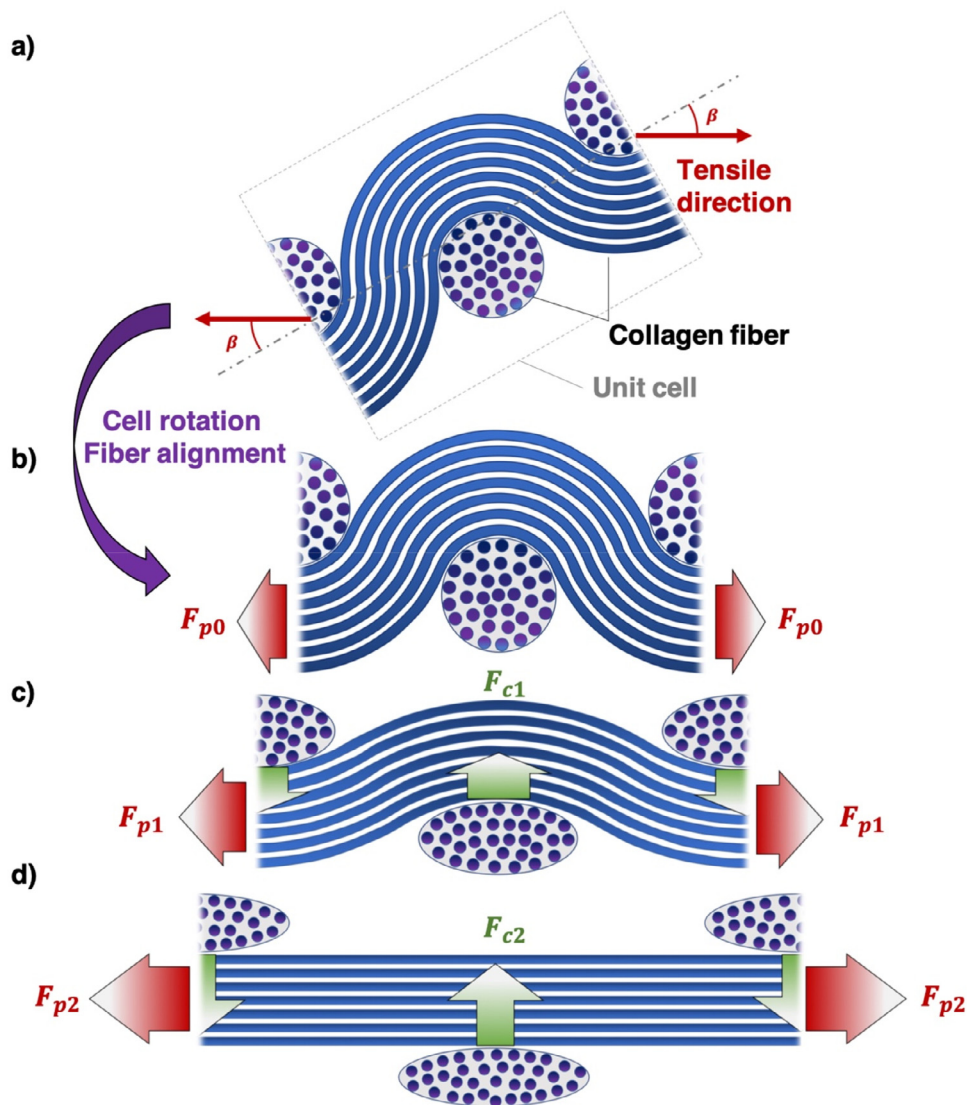


Fig. 3. Schematic description of the process of collagen fiber realignment and straightening, with a transverse resistance due to perpendicular fibers. (a) Periodic unit cell, composed of an S-shaped collagen fiber embedded in the ground substance, surrounded by perpendicular fibers lodged in the concave portions. The cell is initially oriented with an angle β with respect to the tensile direction. (b) A first step of the deformation process is the rotation of the unit cell in the direction of the applied load. This occurs only at the expense of the ground substance. (c) As the fiber straightens, the other transverse fibers resist to this process and deform, conforming to the change in curvature of the pulled fiber. They apply a force with a resultant perpendicular to the neutral axis of the unit cell. (d) Configuration with a fully taught fiber.

simply estimated as the ratio between the effective length and the projected initial length on the tensile axis:

$$\lambda_c = \frac{\omega_n^0}{\sin \omega_n^0} \quad (6)$$

- H5 – The action of the transverse fibers acting on the loaded fiber is represented by a linearly distributed force, acting on a delimited linear portion of the fiber, where contact initially occurs. Friction is neglected. A simplified model is presented on Fig. 4c. The force is modeled by a set of idealized linear springs distributed over the contact surface, and is proportional to the transverse displacement of points of contact on the neutral wire. For the sake of simplicity, it is assumed that this force does not compress the fibers, but only acts against the straightening process.

For the resolution of the deformation of a single semicircular fiber, Sherman et al. [16] used a force-based energy approach to derive the stress-strain relationship, described by Eq. (2). Given that the present model expands on this approach, and on the associated numerical resolution, it seemed more appropriate to follow

the same methods. On the other hand, the shear energy associated with the shear interaction assumed in (H2) is simpler to express as a function of shear strain via the relative fibril displacement. For the complete system, the formulation of an energy-based approach can thus become problematic. Moreover, the assumptions of (H5) are more appropriate for a single equivalent fiber. In order to address these difficulties, the problem is treated in two separate steps. First, the straightening process of the fibrils coupled with the shearing interaction of the interstitial matrix is resolved in the absence of transverse fibers, using a strain-based approach in the expression for the internal energy of the system. The obtained solution yields an equivalent bending modulus, which can be attributed to an equivalent fiber. This also enables the evaluation of fiber anisotropy due to the effect of fibril bundling. Next, the problem with transverse contact forces is addressed by replacing the fibrils/matrix structure by the above defined equivalent fiber, using a stress-based approach in the expression of the internal energy. A stress-stretch relationship for the complete collagen structure is thus obtained, through application of energy theorems.

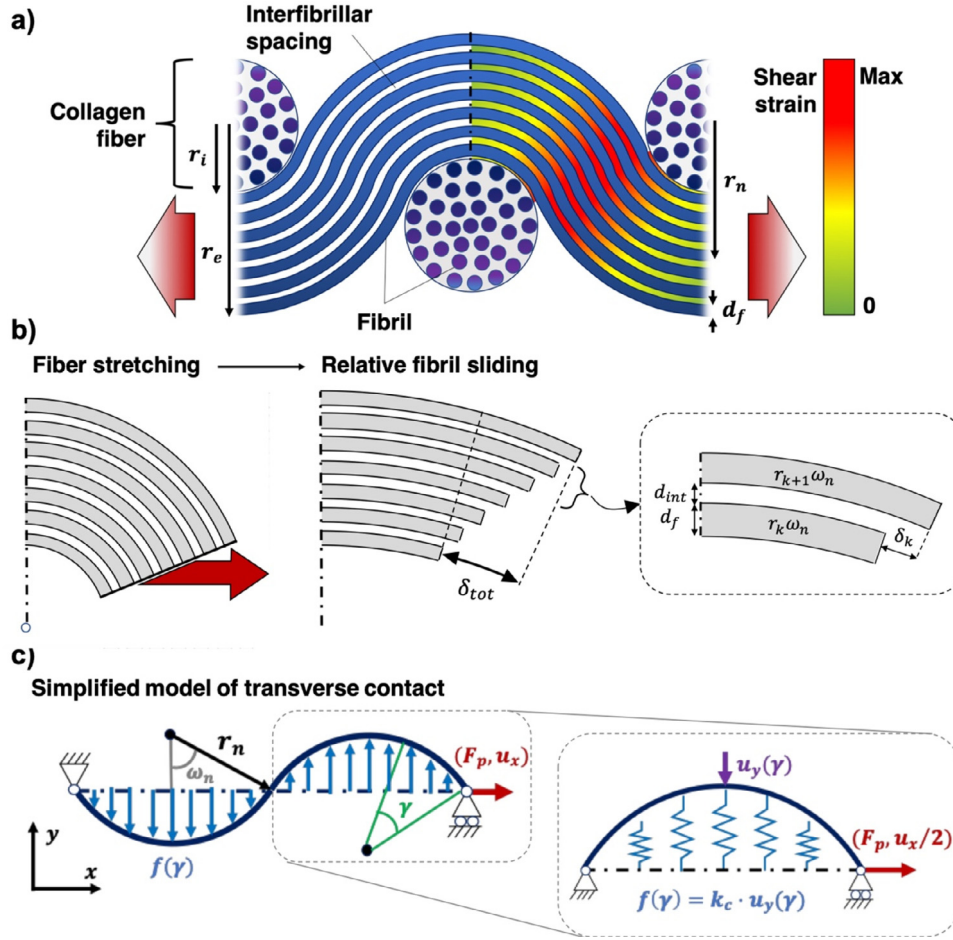


Fig. 4. Mechanical models describing interfibrillar shear and transverse forces. (a) Schematic representation of a fiber being under tension. Due to relative sliding of the fibrils during straightening, shear strain appears in the interfibrillar regions. It is null at the point of inflexion of the fiber and reaches its maximum at ω_n . (b) Sequence illustrating relative sliding between fibrils during fiber stretching. From a portion of fiber spanning 0 to ω_n , it is clear that each fibril portion has a different arc length, defined by $r_k \omega_n$. When stretched, the fibrils do not align along the same opening angle anymore; this mismatch in alignment can be quantified as the relative sliding δ_k . (c) Simplified one-dimensional representation of transverse forces applied on the fiber during stretching. The transverse force is linearly distributed along the concave portion of the fiber, and this force is proportional to the vertical displacement of each contact point, multiplied by a stiffness parameter k_c .

3.4. Equivalent bending stiffness of the fibril bundle structure in the straightening phase

3.4.1. Bending energy of the semi-circular fibrils

It is considered that the deformation process of any fibril in the bundle is equivalent to the deformation of the neutral fibril, with an initial radius of curvature r_n^0 and opening angle ω_n^0 . The contribution of all the fibrils is then obtained by summation of the bending energies. The study of the deformation of a single fibril can be further reduced to the analysis of one semi-circular portion of the S-shape, using a one-dimensional curved beam analogy. It is also convenient to introduce the fibril curvature $\rho_n = 1/r_n$.

Following the incremental approach of Gao et al. [45], we consider two successive deformation states, denoted by $t - 1$ and t . The increment in bending energy of the fibril ΔU_{Bf} is expressed as follows:

$$\Delta U_{Bf} = \frac{1}{2} \int_{-\omega_n^0}^{\omega_n^0} E_f I (\rho_n^t - \rho_n^{t-1})^2 r_n^0 d\theta_n^0 \quad (7)$$

The total internal energy of the structure is the sum of the bending energies of all the fibrils in the fiber, as well as the shearing energies between all interfaces, which need to be expressed.

3.4.2. Shearing energy due to relative fibril sliding

As stated in (H2), relative displacements occur between fibrils during the straightening phase, resulting in shear strains in the matrix. This process is illustrated in Fig. 4a,b: for a portion of the fiber delimited by $[0, \omega_n^{t-1}]$, the arc length of each fibril segment is conserved during fiber straightening (as imposed by (H3)), such that in the deformed configuration, associated with a decrease in curvature, there is relative sliding δ_k between the k -th and the $(k + 1)$ -th fiber, as Fig. 4b shows. The relative displacement of the k -th fibril with respect to the neutral fibril $\Delta \delta_{k/n}$ at an angle $\theta_n^{t-1} \leq \omega_n^{t-1}$ between the deformation states $t - 1$ and t can be quantified by comparing the expected arc length at t with the unchanged effective length of the arc:

$$\Delta \delta_{k/n} = r_k^t \theta_n^t - r_k^{t-1} \theta_n^{t-1} \quad (8)$$

Thus, the relative sliding between two adjacent fibrils is the difference between their relative displacement with the neutral fibril:

$$\Delta \delta_k = \Delta \delta_{k+1/n} - \Delta \delta_{k/n} = (r_{k+1}^t - r_k^t) \theta_n^t - (r_{k+1}^{t-1} - r_k^{t-1}) \theta_n^{t-1} \quad (9)$$

Since $r_{k+1} - r_k = d_f + d_{int}$ at all times (according to (H1)), and $r_n^t \theta_n^t = r_n^0 \theta_n^0$ the expression of $\Delta \delta_k$ can be further simplified as:

$$\Delta \delta_k = \frac{1}{4} (d_f + d_{int}) r_n^0 \theta_n^0 (\rho_n^t - \rho_n^{t-1}) \quad (10)$$

The increment of shear strain $\Delta\gamma_k$ between two successive fibrils is hence defined by:

$$\Delta\gamma_k(\theta_0, r_n) = \frac{\Delta\delta_k(\theta_0, r_n)}{4d_{int}} = \frac{(d_f + d_{int})}{4d_{int}} r_n^0 \theta_n^0 (\rho_n^t - \rho_n^{t-1}) \quad (11)$$

Thus, the increment of shear energy ΔU_{sh}^k between two successive fibrils k and $k + 1$ is:

$$\Delta U_{sh}^k = \int_0^{\omega_n^0} G_m \Delta\gamma_k^2 r_n^0 d_f d_{int} d\theta_n^0 \quad (12)$$

Note that it is assumed that the shear interaction takes place over a cross-section delimited by $d_f d_{int}$. The total increment of shear energy is obtained by summation over the number of interfaces between fibrils. With no dependence in k , this is simply calculated by multiplying ΔU_{sh}^k by $(n_f - 1)$.

3.4.3. Total internal energy of the system

The total change in internal energy ΔU between the states $t - 1$ and t of the fiber structure is the sum of the bending energies of all the fibers, and the shear energies in every interstice:

$$\Delta U = n_f \Delta U_B^f + (n_f - 1) \Delta U_{sh}^k \quad (13)$$

For a virtual displacement δu_x on the fiber, a force ΔF_p is required, resulting in an external work $\delta W_e = \Delta F_p \cdot \delta u_x$. This is associated with variations in bending energy and shear energy, that need to be developed. First, we have:

$$\begin{aligned} \delta(\Delta U_B^f) &= \int_{-\omega_n^0}^{\omega_n^0} E_f I (\rho_n^t - \rho_n^{t-1}) \delta\rho r_n^0 d\theta_n^0 \\ &= \frac{1}{2} E_f I L_f (\rho_n^t - \rho_n^{t-1}) \delta\rho \end{aligned} \quad (14)$$

Next, the variation in shear energy is expressed as follows:

$$\delta(\Delta U_{sh}^k) = 2 \int_0^{\omega_n^0} G_m \Delta\gamma_k \delta\gamma_k r_n^0 d_f d_{int} d\theta_n^0 \quad (15)$$

By using the expression for $\Delta\gamma_k$, and with the following differentiation:

$$\delta\gamma_k = \frac{(d_f + d_{int})}{4d_{int}} r_n^0 \theta_n^0 \delta\rho \quad (16)$$

The variation in shear energy can be obtained by integration:

$$\begin{aligned} \delta(\Delta U_{sh}^k) &= 2 G_m r_n^0 \frac{d_f (d_f + d_{int})^2}{4d_{int}} \int_0^{\omega_n^0} (\rho_n^t - \rho_n^{t-1}) \delta\rho \theta_n^0 d\theta_n^0 \\ &= \frac{G_m L_f^3}{96} \frac{d_f (d_f + d_{int})^2}{d_{int}} (\rho_n^t - \rho_n^{t-1}) \delta\rho \end{aligned} \quad (17)$$

Hence, the variation in internal energy can be rewritten as:

$$\delta(\Delta U) = \left[\frac{1}{2} n_f E_f I L_f + (n_f - 1) \frac{G_m L_f^3}{96} \frac{d_f (d_f + d_{int})^2}{d_{int}} \right] (\rho_n^t - \rho_n^{t-1}) \delta\rho \quad (18)$$

Moreover, following Eq. (5) in (H3), $\delta\rho$ can be expressed as a function of the virtual displacement δu_x :

$$\delta\rho = \frac{\rho_n^{t2}}{4(\omega_n^t \cos(\omega_n^t) - \sin(\omega_n^t))} \delta u_x \quad (19)$$

According to the principle of complementary virtual work, the variation in external work $\delta W_e = \Delta F_p \delta u_x$ is equal to the variation of the internal energy $\delta(\Delta U)$. Hence, the increment of force ΔF_p is obtained by isolating the factor in front of δu_x in the expression of $\delta(\Delta U)$:

$$\Delta F_p = \left[\frac{1}{2} n_f E_f I L_f + (n_f - 1) \frac{G_m L_f^3}{96} \frac{d_f (d_f + d_{int})^2}{d_{int}} \right]$$

$$\times \frac{\rho_n^{t2}}{4(\omega_n^t \cos(\omega_n^t) - \sin(\omega_n^t))} (\rho_n^t - \rho_n^{t-1}) \quad (20)$$

By introducing $\Delta\rho = \rho_n^t - \rho_n^{t-1}$, the apparent stiffness of the system between states $t - 1$ and t can be defined:

$$\begin{aligned} \frac{\Delta F_p}{\Delta\rho} &= \left[\frac{1}{2} n_f E_f I L_f + (n_f - 1) \frac{G_m L_f^3}{96} \frac{d_f (d_f + d_{int})^2}{d_{int}} \right] \\ &\times \frac{\rho_n^{t2}}{4(\omega_n^t \cos(\omega_n^t) - \sin(\omega_n^t))} \end{aligned} \quad (21)$$

We consider that the states $t - 1$ and t are sufficiently close to approximate the ratio above with the tangent stiffness of the system, i.e. $\Delta F_p / \Delta\rho \sim \partial F_p / \partial\rho$.

3.4.4. Equivalent homogenous fiber

We now assume that the fibril/matrix structure can be assimilated to an equivalent homogenous fiber, with bending modulus $(EI)_{eq}$, and the same effective length L_f . In this case, the deformation of the fiber is only dictated by the bending energy. By using a similar reasoning to the one developed above, it can be shown that:

$$\frac{\Delta F_p}{\Delta\rho} = \frac{1}{2} (EI)_{eq} L_f \frac{\rho_n^{t2}}{4(\omega_n^t \cos(\omega_n^t) - \sin(\omega_n^t))} \quad (22)$$

By analogy with the fibril bundle structure, an equivalent bending modulus of the fiber is defined, from Eqs. (21) and (22):

$$(EI)_{eq} = n_f E_f I + (n_f - 1) \frac{G_m L_f^2}{48} \frac{d_f (d_f + d_{int})^2}{d_{int}} \quad (23)$$

The equivalent bending modulus thus defined can then be used in a stress-based approach to study the effect of the transverse force on the deformation process of the collagen structure.

3.5. Resistance to straightening from transverse fibers

The problem is idealized using the simplified representation in Fig. 4c. A semi-circular fiber with initial radius of curvature r_n^0 , opening angle ω_n^0 , and bending modulus $(EI)_{eq}$ is subjected to an applied force F_p along its neutral axis. Hypotheses (H3), (H4), and (H5) still hold for the equivalent fiber. In particular, the effect of transverse fibers is represented here as a linear contact force, applied on the concave portion of the S-shape beam, as Fig. 4c illustrates. The maximum angle of the contact force ω_f^0 is limited by $\pi/2$, after which the contact does not constrain the fiber from straightening. Here again, we consider an increment of deformation between the states at $t - 1$ and t , associated with curvatures ρ_n^{t-1} and ρ_n^t , such that $\Delta\rho = \rho_n^t - \rho_n^{t-1}$. We assume that $\Delta\rho / \rho_n^t \ll 1$.

The contact force is modeled by an idealized linear spring:

$$\Delta f_c(\gamma^t) = -k_c \Delta u_y(\gamma^t) \quad (24)$$

Where Δf_c is the increment in linear contact force, $\gamma^t \in [-\omega_f^t; \omega_f^t]$, and k_c is the contact stiffness. The vertical displacement $\Delta u_y(\gamma)$ of a point at an angle γ is the difference in vertical distance with the loading axis, between states $t - 1$ and t :

$$\begin{aligned} \Delta u_y(\gamma^t) &= \frac{1}{\rho_n^t} (\cos \gamma^t - \cos \omega_n^t) \\ &- \frac{1}{\rho_n^{t-1}} \left(\cos \left(\frac{\rho_n^{t-1}}{\rho_n^t} \gamma^t \right) - \cos \omega_n^{t-1} \right) \end{aligned} \quad (25)$$

Which after further simplification becomes:

$$\Delta u_y(\gamma^t) \approx \frac{\Delta\rho}{\rho_n^{t2}} (\cos \omega_n^t + \omega_n^t \sin \omega_n^t - \gamma^t \sin \gamma^t - \cos \gamma^t) \quad (26)$$

As a consequence of the addition of the contact force, an additional force ΔF_r maintains the fiber along the loading axis during deformation, with:

$$\Delta F_r = \int_{-\omega_f^t}^{\omega_f^t} \Delta f_c(\gamma^t) r_n^t d\gamma^t$$

$$\Delta F_r = -\frac{2k_c \Delta \rho}{\rho_n^{t^3}} \left[\omega_f^t \cos \omega_n^t + \omega_n^t \omega_f^t \sin \omega_n^t - 2 \sin \omega_f^t + \omega_f^t \cos \omega_f^t \right] \quad (27)$$

The equilibrium of a portion of the fiber, limited by an angle θ_n^t , introduces a normal force ΔN and a moment ΔM , that can be decomposed into contributions from the increment of applied force ΔF_p , the constraining force ΔF_r , and the contact force Δf_c :

$$\Delta N = \Delta N_p + \Delta N_r + \Delta N_c$$

$$\Delta M = \Delta M_p + \Delta M_r + \Delta M_c \quad (28)$$

With:

$$\Delta N_p = -\Delta F_p \cos \theta_n^t$$

$$\Delta N_r = -\Delta F_r \sin \theta_n^t$$

$$\Delta N_c = \sin \theta_n^t \int_{-\omega_f^t}^{\theta_n^t} f_c(\gamma^t) r_n^t d\gamma^t \quad (29)$$

And:

$$\Delta M_p = -\Delta F_p r_n^t (\cos \theta_n^t - \cos \omega_n^t)$$

$$\Delta M_r = \Delta F_r r_n^t (\sin \omega_n^t - \sin \theta_n^t)$$

$$\Delta M_c = \int_{-\omega_f^t}^{\theta_n^t} \Delta f_c(\gamma^t) (\sin \gamma^t - \sin \theta_n^t) r_n^{t2} d\gamma^t \quad (30)$$

The increment in tensile elastic energy ΔU_T can be expressed as follows:

$$\Delta U_T = \int_{-\omega_n^t}^{\omega_n^t} \frac{\Delta N^2}{2E_f A_f} r_n^t d\theta_n^t \quad (31)$$

with $\Delta N^2 = \Delta N_p^2 + \Delta N_r^2 + \Delta N_c^2 + 2\Delta N_p \Delta N_r + 2\Delta N_p \Delta N_c + 2\Delta N_r \Delta N_c$.

Similarly, the change in bending energy ΔU_B of the fiber is expressed as follows:

$$\Delta U_B = \int_{-\omega_n^t}^{\omega_n^t} \frac{\Delta M^2}{2(EI)_{eq}} r_n^t d\theta_n^t \quad (32)$$

with $\Delta M^2 = \Delta M_p^2 + \Delta M_r^2 + \Delta M_c^2 + 2\Delta M_p \Delta M_r + 2\Delta M_p \Delta M_c + 2\Delta M_r \Delta M_c$.

Castigliano's second theorem states that the displacement Δu_x at the point of application of the force ΔF_p can be obtained by taking the derivative of the total elastic energy of the fiber by ΔF_p :

$$\Delta u_x / 2 = \frac{\partial(\Delta U_T)}{\partial(\Delta F_p)} + \frac{\partial(\Delta U_B)}{\partial(\Delta F_p)} \quad (33)$$

Hence, this eliminates the terms that do not contain ΔF_p from Eq. (33). It is also quite trivial to show that the term in $\Delta N_p \Delta N_r$ becomes zero after integration. The remaining terms are therefore ΔN_p^2 , $2\Delta N_p \Delta N_c$ in ΔU_T , and ΔM_p^2 , $2\Delta M_p \Delta M_r$, $2\Delta M_p \Delta M_c$ in ΔU_B . After several integration steps, Eq. (33) can be rewritten:

$$\Delta u_x / 2 = \Delta F_p \left(\frac{\varphi_T(\omega_n^t)}{E_f A \rho_n^t} + \frac{\varphi_P(\omega_n^t)}{(EI)_{eq} \rho_n^{t^3}} \right) - \frac{k_c \Delta \rho}{\rho_n^{t^3}} \left(\frac{\varphi_{TC}(\omega_n^t, \omega_f^t)}{E_f A \rho_n^t} + \frac{(\varphi_{BR}(\omega_n^t, \omega_f^t) + \varphi_{BC}(\omega_n^t, \omega_f^t))}{(EI)_{eq} \rho_n^{t^3}} \right) \quad (34)$$

Where $\varphi_T(\omega_n^t)$, $\varphi_{TC}(\omega_n^t, \omega_f^t)$, $\varphi_P(\omega_n^t)$, $\varphi_{BR}(\omega_n^t, \omega_f^t)$, and $\varphi_{BC}(\omega_n^t, \omega_f^t)$ are functions resulting from the integration of energy terms associated with ΔN_p^2 , $2\Delta N_p \Delta N_c$, ΔM_p^2 , $2\Delta M_p \Delta M_r$, and $2\Delta M_p \Delta M_c$, respectively.

Next, assuming that $\Delta \rho \sim \partial \rho$, $\Delta u_x \sim \partial u_x$, and $\Delta F_p \sim \partial F_p$, and by using Eqs. (19) and (34) can be rearranged:

$$\left[\frac{\partial F_p}{\partial u_x} \right]_B = \left[\frac{\varphi_T}{E_f A \rho_n^t} + \frac{\varphi_P}{(EI)_{eq} \rho_n^{t^3}} \right]^{-1} \times \left[\frac{1}{2} + \frac{k_c}{4\rho_n^t (\omega_n^t \cos \omega_n^t - \sin \omega_n^t)} \left(\frac{\varphi_{TC}}{E_f A \rho_n^t} + \frac{(\varphi_{BR} + \varphi_{BC})}{(EI)_{eq} \rho_n^{t^3}} \right) \right] \quad (35)$$

The subscript *B* is introduced to specify that the expression of the tangent stiffness corresponds to the bending dominated regime, during fiber unfolding.

3.6. Tensile regime of the fibril bundle

Once λ_c is reached (see Eq. (6)), the fiber is fully straightened, and the behavior of the structure is dominated by the tensile response of the fibrils in the bundle. The transverse fibers no longer have an effect on the deformation process, in the absence of transverse displacements. Due to the parallel arrangement of fibrils in the bundle, we have: $F_p = n_f F_f$, where F_f is the equidistributed force per fibril. Thus, for the whole fiber in tension:

$$\left[\frac{\partial F_p}{\partial u_x} \right]_T = n_f \left[\frac{\partial F_f}{\partial u_x} \right]_T = n_f \frac{A_f E_f}{L_f} \quad (36)$$

Where A_f is the cross-sectional area of a fibril, while the subscript *T* refers to the purely tensile state. By introducing $A = n_f A_f$ as the effective area of the fiber, it can be noted that Eq. (35) converges to the same value for $\omega_n^t \rightarrow 0$.

3.7. Apparent modulus of the fiber structure

The stress in the deforming fiber is approximated by $\sigma = F_p/A_e$, where $A_e = H d_f$ is the effective area of the fiber and H is its thickness. As stated in Section 2.2, the applied stretch is separated into two components, namely the stretch required to rotate the fiber in the tensile direction λ_r , which occurs without any applied force, and the stretch applied once the deformation of the fiber is initiated λ_f , with $d\lambda_f = du_x / (4r_n^t \sin \omega_n^t)$. Thus, the apparent modulus of the fiber structure E_{app} is expressed as:

$$E_{app}(\lambda_f) = \frac{\partial \sigma}{\partial \lambda_f} = \frac{4r_n^t \sin \omega_n^t}{H d_f} \frac{\partial F}{\partial u_x} \quad (37)$$

More particularly:

$$E_{app} = \begin{cases} \frac{4r_n^t \sin \omega_n^t}{H d_f} \left[\frac{\partial F_p}{\partial u_x} \right]_B, & \text{if } \lambda_f < \lambda_c \\ \frac{4r_n^t \sin \omega_n^t}{H d_f} n_f \frac{A_f E_f}{L_f}, & \text{if } \lambda_f \geq \lambda_c \end{cases} \quad (38)$$

The total stress-stretch relationship of the fiber structure is then obtained by numerical integration of Eq. (2).

3.8. Constitutive framework of the tensile behavior of the dermis

3.8.1. Experimental dataset

In a recent study [25], uniaxial tensile tests on *ex vivo* samples of porcine skin were conducted, with changes in applied strain rate. Samples were cut parallel (longitudinal) and perpendicular (transverse) to the direction of the spine. For the purpose of the present study, experimental results from 29 uniaxial tensile tests (17 longitudinal and 12 transverse samples), tested under four different strain rates (0.0001 s⁻¹, 0.001 s⁻¹, 0.01 s⁻¹, 0.1 s⁻¹) were extracted to test the ability of the proposed model to capture the nonlinear elastic behavior of skin and time-dependent effects.

3.8.2. Distribution of collagen fibers

As illustrated by the sequence Fig. 3, it is assumed that a representative element lies with an angle β with respect to the tensile direction, where $\beta \in]-90^\circ; 90^\circ[$. In reality, collagen fibers in the dermis follow many different orientations, which have been often described using probability distribution functions, for which angles are either contained in planes parallel to the surface of the dermis [34,40,42,46], or span three dimensions [41–43]. In the present representation of fiber realignment by rotation, there is also no distinction between positive and negative orientations, as well as between in-plane and out-of-plane arrangement, so the range for β can be restrained to $[0; 90^\circ[$. Based on the hypothesis formulated by Ridge and Wright [47], also adopted by Ni Annaidh et al. [40], it is assumed that the distribution of collagen fibers is symmetric about the tensile direction (0°), and that it follows a bimodal normal distribution. To reduce computational cost, angular distribution is discretized in increments of 2.5° , resulting in the following modified distribution function:

$$D(\beta|\beta_m, \sigma_f) = \frac{\exp\left(-\frac{(\beta - \beta_m)^2}{2\sigma_f^2}\right) + \exp\left(-\frac{(\beta + \beta_m)^2}{2\sigma_f^2}\right)}{\sum_{k=1}^{36} \exp\left(-\frac{(2.5\pi k/180 - \beta_m)^2}{2\sigma_f^2}\right)} \quad (39)$$

Where β_m is the average angular orientation, and σ_f is the standard deviation.

3.8.3. Matrix component

With the description of the collagen fiber component, the remainder of the representative element is occupied by the ground substance, described by the neoHookean behavior:

$$\sigma_m(\lambda) = \mu_m \left(\lambda^2 - \frac{1}{\lambda} \right) \quad (40)$$

Where σ_m is the component of the stress applied to the ground substance (or matrix). Note that the derived stress-stretch relationship corresponds specifically to uniaxial tension, which is the type of experiment that the constitutive model is compared to in this study. We assume that the contribution of the elastin network is captured by the matrix component. It is considered that the contributions of the fibers and the matrix in the unit cell can be taken in parallel.

3.8.4. Quasi-linear viscoelastic component

Time-dependent effects in skin are exhibited by a change in tissue response with changes in strain rate (increase of the modulus of the linear region, higher failure stress) [25,48,49], and during stress relaxation [25,44,50]. It is also observed that the loading history of a sample has an impact on the time-dependent behavior. For example, Liu and Yeung [50] showed that the shape of the relaxation curve is affected by the level of strain at which relaxation is initiated. The quasilinear viscoelastic theory (QLV), first introduced by Fung [9], incorporates simultaneously time-dependent effects and loading history-dependence by convolution of the purely elastic response $\sigma_{el}(t)$ with the time derivative of a reduced relaxation function $g(t)$:

$$\sigma(t) = \sigma_{el}(t) + \int_0^t \sigma_{el}(t - \tau) \frac{\partial g(\tau)}{\partial \tau} d\tau \quad (41)$$

Note that this definition of the stress in the QLV theory requires that the time derivatives of $\sigma_{el}(t)$ and $g(t)$ are continuous over the considered interval. In the present constitutive framework, the purely elastic response is obtained by resolution of the stress state for the unit cell, as derived above. A three-term Prony series is used for the reduced relaxation function:

$$g(t) = a + be^{-t/\tau_1} + ce^{-t/\tau_2} \quad (42)$$

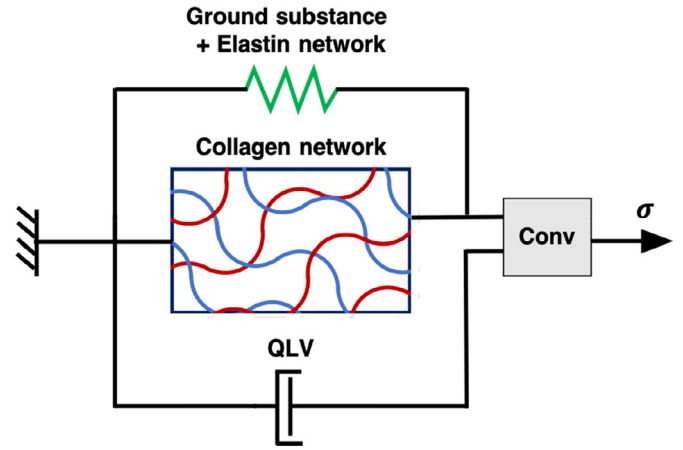


Fig. 5. Schematic representation of the elements of the constitutive model of the dermis. The collagen network, formed by an assembly of distributed collagen fiber structures, is in parallel with the neoHookean ground substance, which also captures the contribution of the elastin network. The time-dependent behavior of the material is modeled by convolution of the elastic response with a reduced relaxation function, as defined by the QLV theory. (For interpretation of the references to colour in this figure legend, the reader is referred to the web version of this article.)

Where (a, b, c) are Prony constants and (τ_1, τ_2) are the time constants of the material, and $g(0^+) = 1$. This is the same reduced relaxation function that was used to fit normalized relaxation plots in [25], for which average values of the constants were reported and showed good consistency.

3.8.5. Constitutive model and parameter identification

The entire constitutive model of the dermis consists of the assembly of the distributed collagen network, with a volume fraction ϕ_c , the neoHookean matrix, with a volume fraction $(1 - \phi_c)$, and the QLV component, for which the time derivative of the reduced relaxation function is convoluted with the elastic response of the structure. This representation is illustrated in Fig. 5, showing the assembly in parallel of the constitutive elements.

The complete resolution of the constitutive model is achieved by summation of the stresses for the elastic component, after numerical integration of Eq. (2), and discrete convolution with the QLV component, equivalent to Eq. (40). This is executed in Matlab.

In total, there are 16 constitutive parameters that need to be identified. These are listed in Table 2, some of which were already listed in Table 1. With such a large parameter set, it becomes difficult to guarantee the uniqueness of a solution that minimizes the optimization problem. In order to facilitate this process, and reduce computational cost, some of these parameters were pre-set, using values that have been reported elsewhere in the literature. This generally concerns parameters for which the reported values are quite consistent, or which have a relatively low influence on the behavior of the model. These are highlighted in bold in Table 2. For example, average values of the reduced relaxation function parameters $(a, b, c, \tau_1, \tau_2)$ were reported in [25] with good consistency, and small standard deviations, without much influence due to sample orientation. For the identified parameters, a physically reasonable range of values is indicated, to assist the optimization algorithm and to reduce the field of search. These values are also indicated at the bottom of Table 2.

Identification of the six remaining parameters is executed using the Parameter Estimation tool in Matlab, by minimization of the Sum Squared Error cost function with a nonlinear least-squares optimization method and a trust-region-reflective algorithm.

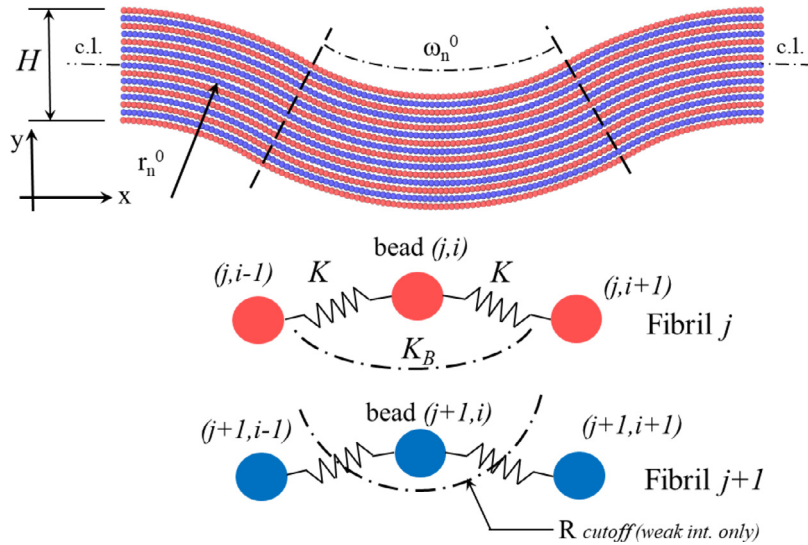


Fig. 6. Initial configuration of the coarse-grained model. An array of collagen fibrils makes a collagen fiber. Each collagen fibril is alternatively colored red-blue-red-blue for visualization purposes. (For interpretation of the references to colour in this figure legend, the reader is referred to the web version of this article.)

Table 2

Summary of the constitutive parameters used in the constitutive model of the dermis. Pre-injected parameters are highlighted in bold, other parameters were calculated with the provided ranges, taken from previous studies, except for G_m , which was roughly estimated based on a reasonable ratio between the straightening phase and the purely tensile regime.

Parameter	Value	Set/Calculated
Collagen volume fraction ϕ_c	0.3 [34,46]	Set
Fiber thickness H	2.5 μm [25]	Set
Fibril diameter d_f	80 nm [25]	Set
Fibril density D_f	0.7 [25]	Set
Fiber initial curvature r_n^0	5 μm [25]	Set
Matrix shear modulus μ_m	1 kPa [34]	Set
Prony constant a	0.6 [25]	Set
Prony constant b	0.21 [25]	Set
Time constant τ_1	12.9 s [25]	Set
Time constant τ_2	1.05 s [25]	Set
Collagen fibril stiffness E_f	30–1570 MPa [38]	Calculated
Fibril interspace shear modulus G_m	0–10 MPa	Calculated
Fiber initial crimp angle ω_n^0	0°–60° [25]	Calculated
Fiber average orientation β_m	0°–90°	Calculated
Orientation standard deviation σ_f	0.01–1	Calculated
Transverse stiffness k_c	0–0.1 N/m ²	Calculated

3.9. Coarse-grained model of collagen fibers

Molecular dynamics computations are a powerful tool and can capture essential aspects of the physical phenomena. In the present case a coarse-grained model, based on a simple elastic network [51–54] and inspired from studies of Arapaima fish scales by Yang et al. [55], was used to theoretically investigate the mechanisms of the deformation in a two-dimensional S-shape curved collagen fiber under uniaxial tension, equivalent to the continuum description developed in Section 3.4. In order to capture the essential physics at an acceptable scale, the collagen fiber consists of an array of adjacent collagen fibrils (see Fig. 6), whereby each collagen fibril is modeled as a series of beads connected by harmonic springs. The initial inter-bead distance is $r_0 = 82$ nm, which is the same as the average diameter of collagen fibrils d_f , as reported from electron microscopy images. Since the density of collagen is $1.34 \cdot 10^3$ kg/m³, the mass of each bead is equal to $5.8 \cdot 10^{-15}$ kg. The total deformation energy of the simulation system is given by:

$$U_{total} = U_T + U_B + U_{weak} \quad (43)$$

where U_T , U_B and U_{weak} are the energies of all pair wise, three-body and weak inter-fibril interactions, respectively, such that:

$$U_T = \sum_{pair} \varphi_T(r) \quad (44)$$

$$\varphi_T(r) = K(r - r_0)^2$$

$$K = \frac{E_f A}{2r_0}$$

K being the stiffness of the pair wise interaction spring between neighboring beads on the same fibril, e.g. beads $((j, i - 1), (j, i))$ as illustrated on Fig. 6. K is estimated from the Young's modulus E_f and the cross-section area A of the collagen fibril. The triplet energy is expressed as:

$$U_B = \sum_{triplets} \varphi_B(r) \quad (45)$$

$$\varphi_B(r) = K_B(\theta - \theta_0)^2$$

$$K_B = \frac{7 E_f \pi d_f^4}{32 r_0}$$

K_B being the bending stiffness of the angular spring of the triplet of beads. Finally, the weak inter-bead energy is defined as:

$$U_{weak} = \sum_{r < r_{cutoff}} \varphi_{weak}(r) \quad (46)$$

$$\varphi_{weak}(r) = 4\epsilon [(\sigma/r)^{12} - (\sigma/r)^6]$$

Where ϵ is the interaction energy between to inter-fibril beads that is given by $\epsilon = d_f r_0 \gamma$ where γ is the surface energy of the collagen fibrils, and $\sigma = d_e / \sqrt[6]{2}$, the equilibrium distance between two neighboring fibrils, so that $d_e = d_f + d_{int}$. To ensure that each collagen fibril only interacts with its nearest neighbors in adjacent fibrils $(j, j + 1)$, the cutoff of the interaction is set as $r_{cutoff} = 1.1d_e$. For full derivation of Eqs. (43) through 46, the reader is referred to references [51–54].

For the sake of simplicity, the model is two-dimensional, and inspired by electron microscopy images (see Fig. 1). In this concept-case study, our model fiber is made of 15 adjacent collagen fibrils with an inter-fibril separation of $d_e = d_f + d_{int} \approx 120$ nm, for a total thickness of 1.8 μm . We include periodic boundary conditions in the direction parallel to the principal axis of the fiber, hence assuming fiber continuity. Prior to deformation, the fibril bundle was minimized and relaxed for 100,000 integration steps.

Uniaxial tensile strain was applied to the entire multi-fibrillar arrangement in a quasi-static manner. For every deformation increment, a uniaxial strain of 0.004 was applied to the model, carrying out energy minimization and equilibrium for 100,000 integration steps. The stress-strain response of the structure during deformation was recorded. In order to visualize and quantify relative sliding of fibrils, the deformation of all the collagen fibrils during the entire loading process was monitored. Simulations were carried out with LAMMPS [56], and visualization was performed using OVITO [57].

4. Predictions of models and comparison with experimental results

4.1. Parameter influence on the fiber structure model

Fig. 7 shows the effect of different constitutive parameters on the stress-strain response of the two-dimensional fibril bundle structure, in the absence of the surrounding ground substance. As expected, the Young's modulus of the fibrils E_f mainly affects the stiffness in the purely tensile region, as shown in Fig. 7a. Because the combined stiffness of the fibrils is divided by the effective area of the fiber ($A_f = Hd_f$), the measured slope is smaller compared to the value of E_f . In contrast, the shear modulus of the inter-fibrillar matrix G_m mainly affects the stiffness of the structure in the straightening phase Fig. 7b). The contact stiffness k_c caused by the structural entanglement has a comparable effect on the straightening phase, except that it also triggers an earlier activation of the purely tensile regime (Fig. 7c). This can be explained by the fact that for a certain threshold of the contact force, resistance to unfolding becomes too large and the tensile component dominates, which can be assimilated to the tightening effect that is seen in braided structures (see Fig. SI I) The value of the initial radius of curvature r_n^0 of the neutral fibril has a similar effect on the stress-strain curve (Fig. 7d), because r_n^0 is mainly a scaling parameter of the fiber, as no notable effect of the fiber thickness H was observed. With a fixed opening angle ω_n^0 (in this case $\omega_n^0 = 30^\circ$), a larger radius simply provides a larger contact length for the linearly distributed contact force f_c . This further justifies the pre-setting of r_n^0 and H is the parameter estimation, and to avoid coupled effects with the identification of k_c . On the other hand, a variation of the initial opening angle ω_n^0 directly impacts the undulation of the semicircular fiber and thus affects the transition from unfolding to tensile regime, as Eq. (6) describes (Fig. 7e). As prescribed by Eqs. (1) and (2), the fiber alignment angle β simply offsets the initiation of the deformation process, as Fig. 7f shows. Hence, with distributed fibers (see Eq. (39)), the process of gradual fiber recruitment can be captured, which also affects the nonlinearity of the J-curve.

4.2. Tensile behavior of the coarse-grained model

4.2.1. Deformation sequence

For comparison purposes, a series of simulations was performed with different Young's moduli for the collagen fibrils, namely 0.5 GPa and 1.0 GPa, which is within the average estimates from collagen fibrils from both computational and experimental approaches [38,58]. The value of $1\text{J}/\text{m}^2$ was attributed to the surface energy of the inter-fibrillar weak interaction. Although it is expected that this energy depends on the degree of hydration, mineral composition and protein sequence, among other factors, the selected value is within the standard range that is found in the literature [38].

Using the present model, one might obtain a diversity of stress-strain curves by using different geometrical parameters (e.g. fibril diameter, fiber radius, fiber opening angle) and collagen

mechanical properties (e.g. surface energy, elastic moduli, etc.). Such a parametric study is beyond the scope of the present work and is left for future research.

Instead, a first assessment of the model is proposed by modifying the value of E_f (0.5 GPa and 1.0 GPa) which in turns affects the tensile and bending stiffness through Eqs. (44) and 45, respectively. As Fig. 8 shows, the coarse-grained tensile responses follow a typical J-curve shape, with a first stage where the load slightly increases as the fiber unfolds from its most curved configuration ($0 < \varepsilon < 0.04$), with a bending dominated behavior through K_B . As the strain keeps increasing ($0.04 < \varepsilon < 0.07$, Stage II), the fiber not only continues straightening but stretching starts playing an important role, so the slope of the loading curve increases. Finally, in stage III ($\varepsilon > 0.07$), the fiber is fully taut and deformation is mostly dominated by the constant K of the pair-wise interaction. The rather wavy behavior of the loading curve for $0 < \varepsilon < 0.07$ can be understood by tracking the trajectory of the beads over time (strain), see Fig. 9.

For the magnitude of strain attained in this simulations, the stresses on each fibril are within the experimental values of single fibril stress-strain experiments by Shen et al. [59]. By comparing the simulation snapshots shown in Fig. 9 and its accompanying schematics, one can better interpret the deformation process. Starting from the initial semicircular undeformed configuration, the application of subsequent strain steps is accommodated by three concurrent effects, in a manner similar to the analytical model: (a) straightening of the fiber comprised of circular segments, producing the rotation of transverse sections; (b) chain extension through separation of neighboring beads due to the tensile strain (stretching); (c) sliding between neighboring fibrils (shearing), as suggested by the description of relative sliding (Fig. 4a-b). The latter effect is not homogeneously distributed across the entire section, but rather takes place as discrete bursts, which are quite marked for tags B-B', C-C' and, to a lesser extent, A-A'. There are other parts e.g. above A' or below C', where shear is homogeneously distributed. The total displacement between the left-topmost and the right-bottommost green beads is of the order of $0.9\ \mu\text{m}$ for an applied strain of $\varepsilon = 0.14$, past the complete unfolding of the fiber. From the value of the initial parameters used for this simulation, the analytical description of shear, described in Section 4.3.2, predicts a final cumulative relative sliding displacement of $\sim 0.89\ \mu\text{m}$, which is in excellent agreement with the measured value.

4.2.2. Comparison with the analytical description

The CG approach shares some features with the analytical model, such as the consideration of a tensile stiffness and bending stiffness but also a considerable difference, which is notorious after inspection of Eq. (46). In the proposed CG approach, cohesion in the collagen fiber is provided by the weak interaction between beads from adjacent fibrils, which is different to the continuous shear occurring in the interstitial matrix in the analytical description. This can be rationalized as the effect of inter-fibril crosslinking acting on the fiber and preserving its shape, also acting during deformation.

The tensile response of the above described coarse-grained fiber for $E_f = 1\ \text{GPa}$ is compared with the response of the continuum representation, resolved in the absence of resistive forces due to transverse fibers ($k_c = 0\ \text{MPa}$) in Fig. 10. For the same initial conditions, i.e. $E_f = 1\ \text{GPa}$; $r_n^0 = 5\ \mu\text{m}$; $\omega_n^0 = 30^\circ$; $H = 1.8\ \mu\text{m}$; $d_f = 82\ \text{nm}$; $D_f = 0.7$, the analytical model (gray dotted line in Fig. 10) shows an earlier transition from the unfolding phase to the tensile regime, and a stiffer linear behavior compared to the atomistic simulation (blue circles). The former can be explained by the fact that in the coarse-grained simulation, initial equilibration (minimization and relaxation) of the structure slightly affects the

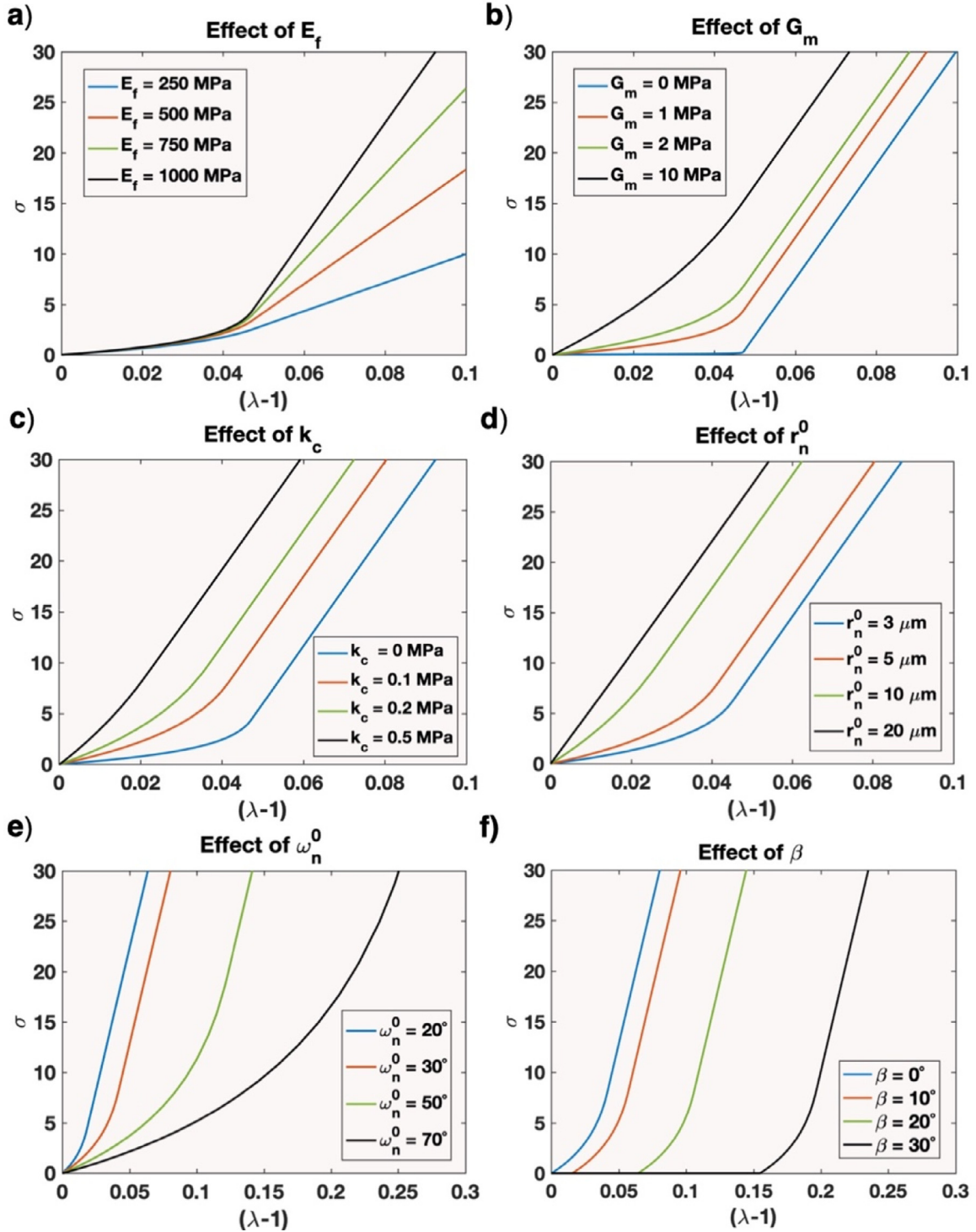


Fig. 7. Effect of different parameters of the fiber structure model on the stress-strain response. Parameters $H = 3$ μm ; $d_f = 80$ nm; $D_f = 0.7$; are maintained constant for all simulations. (a) Effect of the collagen fibril Young's modulus E_f , for $G_m = 1$ MPa; $k_c = 0$ kPa; $r_n^0 = 5$ μm ; $\omega_n^0 = 30^\circ$; $\beta = 0^\circ$. (b) Effect of the interfibrillar shear modulus G_m , for $E_f = 1$ GPa; $k_c = 0$ kPa; $r_n^0 = 5$ μm ; $\omega_n^0 = 30^\circ$; $\beta = 0^\circ$. (c) Effect of the contact stiffness parameter k_c , for $E_f = 1$ GPa; $G_m = 1$ MPa; $r_n^0 = 5$ μm ; $\omega_n^0 = 30^\circ$; $\beta = 0^\circ$. (d) Effect of the initial neutral radius of curvature r_n^0 , for $E_f = 1$ GPa; $G_m = 1$ MPa; $k_c = 0.1$ MPa; $\omega_n^0 = 30^\circ$; $\beta = 0^\circ$. (e) Effect of the initial opening angle of the neutral fibril ω_n^0 , for $E_f = 1$ GPa; $G_m = 1$ MPa; $k_c = 0.1$ MPa; $r_n^0 = 5$ μm ; $\beta = 0^\circ$. (f) Effect of the initial orientation between the principal axis of the fiber and the tensile direction, described by the angle β , for $E_f = 1$ GPa; $G_m = 1$ MPa; $k_c = 0.1$ MPa; $r_n^0 = 5$ μm ; $\omega_n^0 = 30^\circ$.

geometry of the S-shape, and thus the opening angle. Estimates show that the opening angle of the semi-circular portion after relaxation is closer to 37° (see Supporting Information (SI) II). Thus, the value of ω_n^0 in the continuum (analytical) model was modified accordingly, and as a result the red curve in Fig. 10 more accurately

captures the unfolding-stretching transition of the coarse-grained model. The value of the fibril Young's modulus was adjusted to $E_f = 0.92$ GPa to better fit the linear regime. In the coarse-grained model, the tensile modulus is slightly below the prediction, presumably due to effects of the weak interaction (Eq. (46)), when

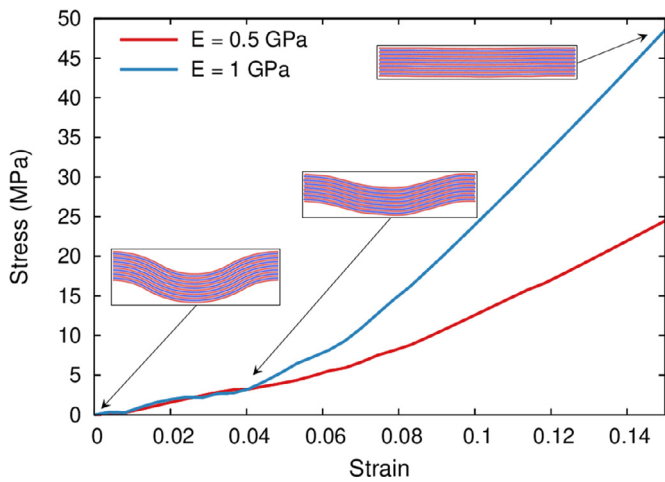


Fig. 8. Loading curves showing the influence of Young's modulus. Visualization of the intermediate configuration for a strain of 0.04 shows what seems and uneven deformation state. Reasons explained in main text.

the bead-to-bead distance increases (i.e. while the pairwise interaction is dictated by a harmonic spring, the weak interaction obeys a Lennard-Jones potential law with a different power law to that of a spring. It is reasonable to expect a slight deviation from the theoretical value associated to the pairwise spring). Notwithstanding these adjustments, Fig. 10 shows that a very good agreement is obtained between the responses of the atomistic model and of the adjusted continuum representation, for an interfibrillar shear modulus of $G_m = 5$ MPa.

Given that the most important contribution of the CG model presented here is, perhaps, the consideration of the geometrical aspects of fibril/fiber arrangement in skin, most of the collagen mechanical constants used in our study were taken to match experimental records. Further parametric studies are needed to fully assess the potential of the proposed CG model. Corr and Hart [60] determined the mechanical properties of scar tissue in porcine skin and observed that it has a different mechanical response,

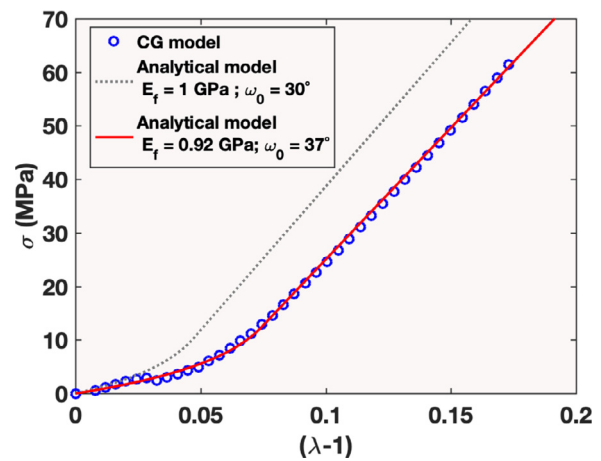


Fig. 10. Comparison of the stress-strain curves obtained for the coarse grained (CG) atomistic model, and the analytical model with equivalent initial values (gray dotted curve), and with adjusted parameters (red curve), showing a better agreement between both descriptions. The optimal value of 5 MPa was used for G_m . (For interpretation of the references to colour in this figure legend, the reader is referred to the web version of this article.)

characterized by a greatly reduced failure stress, reduced low-load compliance, and altered fiber directionality. Our coarse grain model can help us to assess the changes in skin response as changes occur.

4.3. Parameter identification from the constitutive framework

The Parameter Estimation tool in Matlab determines the optimal values for the set of parameters listed in Table 2, for each given experimental curve. Examples for one longitudinal sample and one transverse sample, tested at a strain rate of 10^{-3} s^{-1} , are shown in Fig. 11. The constitutive model matches very well the different deformation stages of the J-curve of skin, with coefficients of determination R^2 above 0.99. This is in majority due to

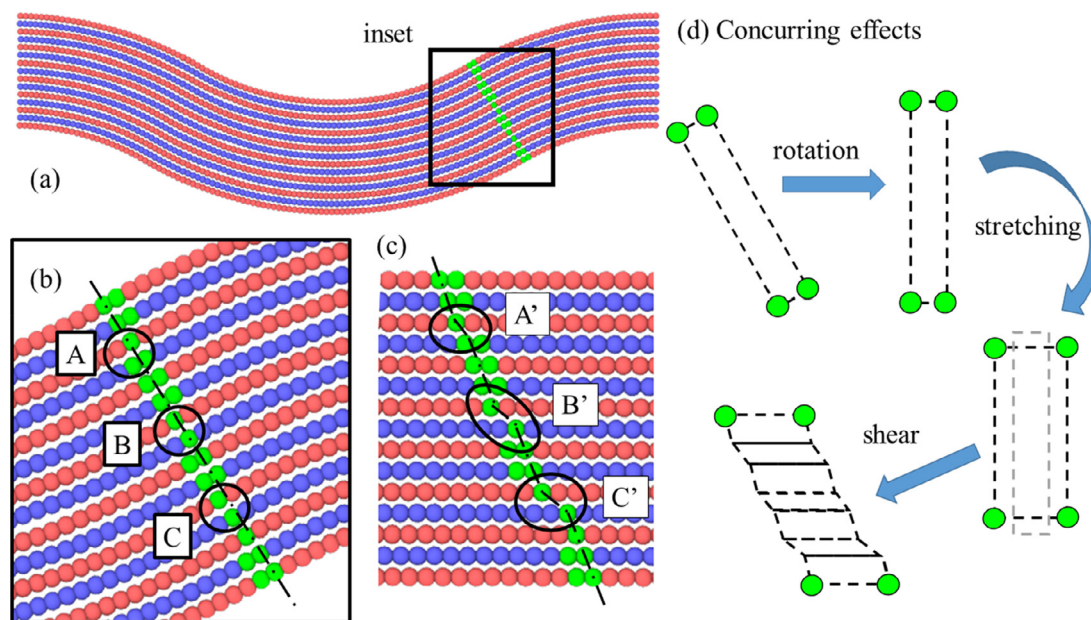


Fig. 9. (a) The inflection section of the bi-curved fiber is identified and tracked during deformation. (b) and (c) present the initial configuration and its $\epsilon=0.14$ counterpart, corresponding to a fully stretched state. Note the changes A-A', B-B' and C-C'. The deformation can be interpreted as the result of three concurring effects, rotation of the section, stretching and shear.

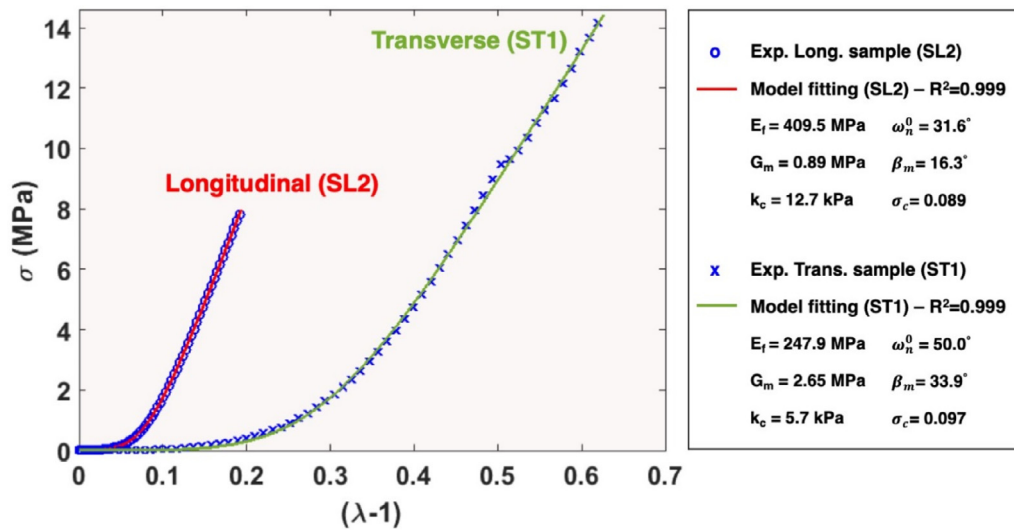


Fig. 11. Performance of the model with two selected experimental (Exp.) curves, a longitudinal sample (SL2), and a transverse sample (ST1), both tested at a strain rate of $10^{-3}s^{-1}$. Fitted curves display the good ability of the model to capture the nonlinear elastic behavior of skin for two perpendicular orientations. The legend on the side of the graph also indicates the identified values of the constitutive parameters.

Table 3

Average values \pm S.D. of the constitutive parameters after curve fitting of experimental results, sorted by sample orientation (17 longitudinal samples and 12 transverse).

	Longitudinal (Mean \pm S.D.)	Transverse (Mean \pm S.D.)	Total (Mean \pm S.D.)
E_f	420.4 \pm 138.1 MPa	435.0 \pm 165.2 MPa	426.5 \pm 147.2 MPa
G_m	1.31 \pm 0.87 MPa	2.02 \pm 1.84 MPa	1.61 \pm 1.37 MPa
k_c	14.1 \pm 11.4 kPa	47.0 \pm 56.2 kPa	27.7 \pm 39.9 kPa
ω_n^0	36.7° \pm 5.3°	39.5° \pm 8.4°	37.9° \pm 6.8°
β_m	20.5° \pm 4.94°	29.6° \pm 10.1°	24.2° \pm 8.6°
σ_f	0.084 \pm 0.040	0.244 \pm 0.318	0.150 \pm 0.217

Table 4

Spearman correlation analysis of the six identified constitutive parameters, also compared to the applied strain rate and sample orientation. The spearman rho coefficient (in **bold**) indicates the strength and the direction of the correlation, while the p-value (in *italic*) provides the significance (*= p -value<5%).

	E_f	G_m	k_c	ω_n^0	β_m	σ_c
G_m	-0.342 <i>0.069</i>					
k_c	0.275 <i>0.148</i>	0.120 <i>0.536</i>				
ω_n^0	-0.321 <i>0.090</i>	0.440 <i>0.017*</i>	-0.178 <i>0.355</i>			
β_m	-0.259 <i>0.175</i>	0.261 <i>0.171</i>	0.105 <i>0.586</i>	0.493 <i>0.007*</i>		
σ_c	0.071 <i>0.715</i>	0.139 <i>0.471</i>	0.009 <i>0.962</i>	-0.057 <i>0.769</i>	0.291 <i>0.126</i>	
Strain rate	0.155 <i>0.422</i>	-0.113 <i>0.560</i>	0.057 <i>0.770</i>	0.015 <i>0.939</i>	0.181 <i>0.348</i>	0.039 <i>0.842</i>
Orientation	0.008 <i>0.966</i>	0.209 <i>0.276</i>	0.209 <i>0.276</i>	0.071 <i>0.714</i>	0.427 <i>0.021*</i>	0.393 <i>0.035*</i>

the combined contribution of the gradual realignment of collagen fibers and the straightening process which the model captures.

The complete dataset of identified parameters for all experimental curves is provided in SI III. For the sake of conciseness, only average values and standard deviations for transverse and longitudinal sample orientations are presented in Table 3. Additionally, a Spearman rho correlation analysis was conducted in order to identify potential correlations between the constitutive parameters, as well as the experimental conditions, i.e. sample orientation and applied strain rate (see Table 4), and a parameter sensitivity analysis is also detailed in SI III, identifying the parameters with the highest influence on the response of the model. At first glance, it is interesting to point out that the applied strain rate does not

correlate with any of the estimated parameters, suggesting that the QLV component adequately captures the time-dependent behavior of the tissue.

An average Young's modulus of 426.5 ± 147 MPa was found for collagen fibrils, which falls in the lower range of experimentally reported values [38]. Intrinsic phenomena such as fiber and fibril sliding can contribute in decreasing the apparent stiffness of collagen. Nonetheless, the estimated stiffness is in reasonable agreement with the values found by Jor et al. [46] (~360 MPa) and Meijer et al. [34] (360 MPa – 518 MPa) with the Lanir model. No significant effect of orientation was found, indicating that material anisotropy is dictated by other constitutive parameters. The inter-fibril shear modulus G_m displays rather large variations

($1.61 \pm 1.37 \text{ MPa}$ in total), especially for transverse samples ($2.02 \pm 1.84 \text{ MPa}$), but the average values are about two orders of magnitude below the fibril modulus, as expected from the estimations with the coarse-grained model.

The average curvature of collagen fibers ($\omega_n^0 = 37.9^\circ \pm 6.8^\circ$) is consistent with the measured values for a radius of curvature of $r_n^0 = 5 \text{ }\mu\text{m}$, and does not show any dependence on orientation. An increase in opening angle is significantly correlated with an increase in G_m (p-value = 0.017). This can be interpreted by the effect of a more curved initial state, but also by the notion that with a fixed radius of curvature a larger opening angle increases the effective length of the fiber L_f , and therefore the contact area with the interfibrillar matrix is increased, which could affect the effect shear in a nonlinear fashion.

The calculated average orientation of collagen β_m , $\beta_m^L = 20.5^\circ \pm 4.9^\circ$ for longitudinal samples and $\beta_m^T = 29.6^\circ \pm 10.1^\circ$ for transverse samples, shows a significant correlation (p-value = 0.021) between the initial alignment of collagen fibers and the orientation of the tested sample. However, the difference between both orientations is well below the expected trend, as perpendicular orientations should yield average alignments approximately 90° apart. This observation highlights two limitations of the present representation: a) an increase of the angle β substantially delays the onset of fiber deformation (cf. Fig. 7b), and the gap in response between two subsequent angular increments becomes more pronounced, which yields a more discontinuous response for a higher value of β_m ; b) the proposed fiber distribution imposes symmetry around the loading axis, which may not be a realistic assumption. These shortcomings also explain the highly significant correlation (p-value = 0.007) between β_m and ω_n^0 , which should not be observed, as one is an effect of the loading configuration and the latter is an intrinsic property of the collagen fibers. Still, as both parameters have an effect on the transition of the J-curve, it is understandable that the model finds a correlation between their distinct influences. As mentioned earlier, fiber unfolding and realignment are concurrent processes in skin [37]. It is therefore preferable that one of them would be determined *a priori* in the model, which is also reflected by the sensitivity analysis (see SI IV) which indicates that both parameters have a high influence on the model response.

The standard deviation in fiber distribution σ_c is also an intrinsic property of the sample, and should not be influenced by sample orientation, which is in this case confirmed by a weak correlation between the two. As a direct measure of tissue anisotropy, the standard deviation would probably be more affected by the region of the body from which the sample is extracted, which was not systematically reported for this experimental dataset. As a matter of fact, most skin samples were extracted close to the spine, which is generally less anisotropic compared to other regions [47,61]. In fact, the identified average of $\sigma_c = 0.15 \pm 0.22$ yields an estimated fiber dispersion coefficient [21] that is at least one order of magnitude below other reported values for skin [40,42]. This is another consequence of the strong effect of the initial alignment of fibers in the model. A wider distribution effectively reduces the fraction of collagen fibers that contribute to the deformation process, which is in contradiction with the consistency of the measured stiffness. With a maximum strain of ~ 0.6 prior to failure, following Eq. (1), the maximum angle for which a fiber participates in the response of the tissue is approximately 52° , hence directly eliminating the contribution of fibers with a higher alignment angle. This further indicates that the representation of realignment needs to be refined, and that σ_c should preferably be predetermined, as also suggested by the sensitivity analysis (SI IV).

Finally, the estimated contact stiffness from transverse fibers k_c ($27.7 \pm 39.9 \text{ kPa}$ in total; $14.1 \pm 11.4 \text{ kPa}$ for longitudinal samples; $47.0 \pm 56.2 \text{ kPa}$ for transverse samples) appears to be slightly

affected by sample orientation, however the correlation analysis rejects this hypothesis. It is however possible that a larger cell rotation is more likely to result in highly entangled structures. Current lack of knowledge on the interactions resulting from fiber entanglement in collagenous tissues, and on the transverse stiffness of collagen fibril bundles renders the interpretation of the obtained data more complicated.

5. Conclusions

The present constitutive model of skin proposes a new approach to the mechanical behavior of the dermis, based on observations of the arrangement of the collagenous network. In particular, two microscale characteristics were incorporated:

- The effect of fiber braiding, following recent observations which suggest a certain level of inter-fiber entanglement (see also Figure SI I). Coincidentally, uniaxial tensile tests on braided structures reveal physical features, such as nonlinear elasticity and dissipative behavior, that are reminiscent of some aspects of the tensile behavior of skin;
- The effect of shear at the interface between adjacent fibrils in a fiber bundle, as a result of fiber undulation. This process is prominent in the bending-dominated straightening phase of the fiber.

These characteristics are implemented in the model within a representative element, comprising a two-dimensional semicircular bundle of collagen fibrils, transverse fibers that generate interaction forces opposing to the straightening process, and a surrounding hyperelastic ground substance. The effects of shear are described in the interstitial matrix between the fibrils. The geometry of the unit cell is dictated by the average dimensions of the collagen fiber: fiber thickness $H \approx 2.5 \text{ }\mu\text{m}$, fiber neutral radius of curvature $r_n^0 = 5 \text{ }\mu\text{m}$, opening angle of the circular segment $\omega_n^0 \approx 37.8^\circ \pm 6.8^\circ$, and a fibril diameter $d_f \approx 82 \text{ nm}$. It is important to point out that these dimensions are mostly reflective of an averaged description of collagen fibers, based on observations made in the reticular dermis. Variations in fiber geometry, either due to differences found between the papillary dermis and the reticular dermis, or simply due to the fact that in reality, these dimensions are more sparsely distributed across the tissue, are not represented in the proposed model. With the appropriate knowledge, these aspects could be incorporated with a layered model, or with the implementation of distribution functions for some parameters. This would however introduce additional parameters to the constitutive model that would considerably complicate the parameter estimation, given that the current description already requires the identification of 16 constants, unless some of them are initially pre-set. Hence, the present model assumes that the reticular dermis is mainly responsible for the large strain tensile response of skin, with collagen fibers that follow a similar curved geometry.

The following are the principal results of this investigation:

- Predictions are in reasonable agreement with the tensile response that has been reported elsewhere, either experimentally or with comparable modeling approaches. However, some large variations in the estimated values of some parameters or unexpected trends reveal some limitations of the constitutive framework.
- In the present description, the rotation process of the fibers does not require the application of any force; instead an “alignment” stretch dictates the onset of fiber deformation. During the realignment phase, the ground substance mainly bears the load. This representation is analogous to a fiber network where all fibers are connected by ball-and-socket joints [62]. However, results of the parameter estimation point out that this

representation yields unrealistic effects, where only a reduced portion of the fibers are recruited, or highly concentrated fiber alignments are found. Experiments using in situ small angle x-ray scattering (SAXS) or multiphoton imaging with a tensile setup generally show that a significantly larger population of fibers gets recruited during tensile deformation [37,63,64]. Notwithstanding, still little is known on the actual arrangement of collagen fibers in the dermis, most particularly on the persistence length of the fibers, their respective interactions, and the nature/type of the connection between them. Future work on the topic would provide clues that could inform further improvements of the constitutive model. Moreover, a better knowledge of the arrangement of collagen and its evolution would remove uncertainties in the model caused by fiber orientation and dispersion (or standard deviation), as the results of the sensitivity analysis suggest.

- The time-dependent behavior of the material is described by the quasilinear viscoelastic theory (QLV) theory, with a three-term Prony series relaxation function. Changes in the parameters of the QLV component were not considered in this study, as the approach mainly focuses on the elastic contribution. A notable interest in implementing viscoelasticity was to observe whether the effect of applied strain rate can be entirely captured by this component, without affecting the other structural and elastic parameters. This was then correctly established in the correlation analysis. Besides the fact that some limitations of the QLV theory have been reported for skin [65,66], future developments of the model should aim to replace this component with structural features that incorporate time-dependence and the dissipative behavior of skin. Indeed, the definitions of the interfibrillar shear interaction and of the contact between entangled fibers can be expanded to include viscoelasticity, dissipative behavior, irreversible damages, and friction. Fibril discontinuity should be further studied to account for effects of shear-lag [67]. Lastly, relative sliding between fibers, which could explain the low values that were found for the Young's modulus E_c , were not directly investigated here.
- The proposed coarse-grained model has the potential to allow for a systematic investigation of how different geometric and mechanical characteristics influence the response of fibers to loading, e.g. radius of curvature, fiber thickness, number of fibrils, spanned angle, inter-fibril interaction strength and the stiffness of a single collagen fibril. Moreover, further iterations of the model could incorporate features such as a post-elastic behavior (damage) [68], or irreversible deformations caused by relative displacements of beads, which could be evidenced under cyclical loads.

Funding Agency

This work was supported by the Multidisciplinary University Research Initiative to University of California Riverside, funded by the Air Force Office of Scientific Research (AFOSR-FA9550-15-1-0009), with subcontracts to UC San Diego and UC Berkeley.

Declaration of Competing Interest

None.

Acknowledgements

We thank Professor Katherine Brown, Professor Alum Williams, and Dr. Ben Butler for taking part in the experiments conducted on porcine tissue at Cambridge University. We also thank Dr. Wen Yang and Dr. Haocheng Quan in the precious assistance they have provided in obtaining experimental data and analyzing microscopy

images. CJR thanks M.S. Moyano for help in the development of the code for coarse-grain geometry generation. Lastly, we thank Dr. Markus Buehler and Dr. Zhao Qin for valuable discussions on coarse-grain modeling.

Supplementary materials

Supplementary material associated with this article can be found, in the online version, at doi:[10.1016/j.actbio.2020.01.026](https://doi.org/10.1016/j.actbio.2020.01.026).

References

- [1] G. Limbert, Mathematical and computational modelling of skin biophysics: a review, *Proc. R. Soc. A Math. Phys. Eng. Sci.* 473 (2017) <http://rspa.royalsocietypublishing.org/content/473/2203/20170257.abstract>.
- [2] J.W.Y. Jor, M.D. Parker, A.J. Taberner, M.P. Nash, P.M.F. Nielsen, Computational and experimental characterization of skin mechanics: identifying current challenges and future directions, *Wiley Interdiscip. Rev. Syst. Biol. Med.* 5 (2013) 539–556, doi:[10.1002/wsbm.1228](https://doi.org/10.1002/wsbm.1228).
- [3] S.D. Łagan, A. Liber-Kneć, Experimental testing and constitutive modeling of the mechanical properties of the swine skin tissue, *Acta Bioeng. Biomech. Orig. Pap.* (2017) 19, doi:[10.5277/ABB-00755-2016-02](https://doi.org/10.5277/ABB-00755-2016-02).
- [4] P.A.L.S. Martins, R.M.N. Jorge, A.J.M. Ferreira, A comparative study of several material models for prediction of hyperelastic properties: application to silicone-rubber and soft tissues, *Strain* 42 (2006) 135–147, doi:[10.1111/j.1475-1305.2006.00257.x](https://doi.org/10.1111/j.1475-1305.2006.00257.x).
- [5] W. Li, X.Y. Luo, An invariant-based damage model for human and animal skins, *Ann. Biomed. Eng.* 44 (2016) 3109–3122, doi:[10.1007/s10439-016-1603-9](https://doi.org/10.1007/s10439-016-1603-9).
- [6] R.W. Ogden, Large deformation isotropic elasticity - On the correlation of theory and experiment for incompressible rubberlike solids, *Proc. R. Soc. A Math. Phys. Eng. Sci.* 326 (1972) 565–584, doi:[10.1098/rspa.1972.0026](https://doi.org/10.1098/rspa.1972.0026).
- [7] M. Mooney, A theory of large elastic deformation, *J. Appl. Phys.* 11 (1940) 582–592, doi:[10.1063/1.1712836](https://doi.org/10.1063/1.1712836).
- [8] R.S. Rivlin, Large elastic deformations of isotropic materials. IV. further developments of the general theory, *Philos. Trans. R. Soc. A Math. Phys. Eng. Sci.* 241 (1948) 379–397, doi:[10.1098/rsta.1948.0024](https://doi.org/10.1098/rsta.1948.0024).
- [9] Y.C. Fung, Elasticity of soft tissues in simple elongation, *Am. J. Physiol.* 213 (1967) 1532–1544, doi:[10.1152/ajplegacy.1967.213.6.1532](https://doi.org/10.1152/ajplegacy.1967.213.6.1532).
- [10] G. Limbert, J. Middleton, A transversely isotropic viscohyperelastic material application to the modeling of biological soft connective tissues, *Int. J. Solids Struct.* 41 (2004) 4237–4260, doi:[10.1016/j.ijsolstr.2004.02.057](https://doi.org/10.1016/j.ijsolstr.2004.02.057).
- [11] K.Y. Volokh, Modeling failure of soft anisotropic materials with application to arteries, *J. Mech. Behav. Biomed. Mater.* 4 (2011) 1582–1594, doi:[10.1016/j.jmbbm.2011.01.002](https://doi.org/10.1016/j.jmbbm.2011.01.002).
- [12] E.M. Arruda, M.C. Boyce, A three-dimensional constitutive model for the large stretch behavior of rubber elastic materials, *J. Mech. Phys. Solids* 41 (1993) 389–412, doi:[10.1016/j.commat.2011.01.026](https://doi.org/10.1016/j.commat.2011.01.026).
- [13] E. Kuhl, K. Garikipati, E.M. Arruda, K. Gosh, Remodeling of biological tissue: mechanically induced reorientation of a transversely isotropic chain network, *J. Mech. Phys. Solids* 53 (2005) 1552–1573, doi:[10.1016/j.jmps.2005.03.002](https://doi.org/10.1016/j.jmps.2005.03.002).
- [14] J.S. Bergström, M.C. Boyce, Constitutive modeling of the time-dependent and cyclic loading of elastomers and application to soft biological tissues, *Mech. Mater.* 33 (2001) 523–530, doi:[10.1016/S0167-6636\(01\)00070-9](https://doi.org/10.1016/S0167-6636(01)00070-9).
- [15] J.E. Bischoff, E.M. Arruda, K. Gosh, A rheological network model for the continuum anisotropic and viscoelastic behavior of soft tissue, *Biomech. Model. Mechanobiol.* 3 (2004) 56–65, doi:[10.1007/s10237-004-0049-4](https://doi.org/10.1007/s10237-004-0049-4).
- [16] V.R. Sherman, Y. Tang, S. Zhao, W. Yang, M.A. Meyers, Structural characterization and viscoelastic constitutive modeling of skin, *Acta Biomater.* (2016), doi:[10.1016/j.actbio.2017.02.011](https://doi.org/10.1016/j.actbio.2017.02.011).
- [17] G.A. Holzapfel, R.W. Ogden, S. Sherifova, On fibre dispersion modelling of soft biological tissues: a review, *Proc. R. Soc. A Math. Phys. Eng. Sci.* (2019) 475, doi:[10.1098/rspa.2018.0736](https://doi.org/10.1098/rspa.2018.0736).
- [18] R.B. Groves, S.A. Coulman, J.C. Birchall, S.L. Evans, An anisotropic, hyperelastic model for skin: experimental measurements, finite element modelling and identification of parameters for human and murine skin, *J. Mech. Behav. Biomed. Mater.* 18 (2013) 167–180, doi:[10.1016/j.jmbbm.2012.10.021](https://doi.org/10.1016/j.jmbbm.2012.10.021).
- [19] Y. Lanir, Constitutive equations for fibrous connective tissues, *J. Biomech.* 16 (1983) 1–12, doi:[10.1016/0021-9290\(83\)90041-6](https://doi.org/10.1016/0021-9290(83)90041-6).
- [20] O. Lokshin, Y. Lanir, Viscoelasticity and preconditioning of rat skin under uniaxial stretch: microstructural constitutive characterization, *J. Biomech. Eng.* 131 (2009) 31009, doi:[10.1115/1.3049479](https://doi.org/10.1115/1.3049479).
- [21] T.C. Gasser, R.W. Ogden, G.A. Holzapfel, Hyperelastic modelling of arterial layers with distributed collagen fibre orientations, *J. R. Soc. Interface.* 3 (2006) 15–35, doi:[10.1098/rsif.2005.0073](https://doi.org/10.1098/rsif.2005.0073).
- [22] G. Limbert, A mesostructurally-based anisotropic continuum model for biological soft tissues-Decoupled invariant formulation, *J. Mech. Behav. Biomed. Mater.* 4 (2011) 1637–1657, doi:[10.1016/j.jmbbm.2011.07.016](https://doi.org/10.1016/j.jmbbm.2011.07.016).
- [23] D. Pond, A. McBride, L. Davids, B.D. Reddy, G. Limbert, Constitutive modelling of the skin accounting for chronological ageing, (2017). <http://arxiv.org/abs/1709.03752>.
- [24] J. Wu, H. Yuan, L. Li, K. Fan, S. Qian, B. Li, Viscoelastic shear lag model to predict the micromechanical behavior of tendon under dynamic tensile loading, *J. Theor. Biol.* 437 (2018) 202–213, doi:[10.1016/j.jtbi.2017.10.018](https://doi.org/10.1016/j.jtbi.2017.10.018).

- [25] A. Pissarenko, W. Yang, H. Quan, K.A. Brown, A. Williams, W.G. Proud, M.A. Meyers, Tensile behavior and structural characterization of pig dermis, *Acta Biomater* (2019), doi:10.1016/j.actbio.2019.01.023.
- [26] A. Ni Annaidh, K. Bruyère, M. Destrade, M.D. Gilchrist, C. Maurini, M. Otténio, G. Saccomandi, Automated estimation of collagen fibre dispersion in the dermis and its contribution to the anisotropic behaviour of skin, *Ann. Biomed. Eng.* 40 (2012) 1666–1678, doi:10.1007/s10439-012-0542-3.
- [27] M.F. Leyva-Mendivil, A. Page, N.W. Bressloff, G. Lambert, A mechanistic insight into the mechanical role of the stratum corneum during stretching and compression of the skin, *J. Mech. Behav. Biomed. Mater.* 49 (2015) 197–219, doi:10.1016/j.jmbbm.2015.05.010.
- [28] F.M. Hendriks, D. Brokken, C.W.J. Oomens, D.L. Bader, F.P.T. Baijens, The relative contributions of different skin layers to the mechanical behavior of human skin in vivo using suction experiments, 28 (2006) 259–266. doi:10.1016/j.jmedengphy.2005.07.001.
- [29] C.O. Flynn, B.A.O. McCormack, A three-layer model of skin and its application in simulating wrinkling, *Comput. Methods Biomech. Biomed. Engin.* 12 (2009) 125–134, doi:10.1080/10255840802529933.
- [30] M.S. Christensen, C.W. Hargens, S. Nacht, E.H. Gans, Viscoelastic properties of intact human skin: instrumentation, hydration effects, and the contribution of the stratum corneum, *J. Invest. Dermatol.* 69 (1977) 282–286, doi:10.1111/1523-1747.ep12507500.
- [31] K.S. Wu, W.W. Van Osdol, R.H. Dauskaradt, Mechanical properties of human stratum corneum: effects of temperature, hydration, and chemical treatment, *Biomaterials* 27 (2006) 785–795, doi:10.1016/j.biomaterials.2005.06.019.
- [32] G.L. Wilkes, I.A. Brown, R.H. Wildnauer, The biomechanical properties of skin, *CRC Crit. Rev. Bioeng.* 1 (1973) 453–495 <http://www.ncbi.nlm.nih.gov/pubmed/4581809>.
- [33] Y. Wang, R. Xu, W. He, Z. Yao, H. Li, J. Zhou, J. Tan, S. Yang, R. Zhan, G. Luo, J. Wu, Three-Dimensional histological structures of the human dermis, *Tissue Eng. Part C Methods* 21 (2015) 932–944, doi:10.1089/ten.tec.2014.0578.
- [34] R. Meijer, L.F. a. Douven, C.W.J. Oomens, Characterisation of anisotropic and non-linear behaviour of human skin in vivo, *Comput. Methods Biomech. Biomed. Engin.* 2 (1999) 13–27, doi:10.1080/10255849908907975.
- [35] J.F.M. Manschot, A.J.M. Brakkee, The measurement and modelling of the mechanical properties of human skin in vivo—I. The measurement, *J. Biomech.* 19 (1986) 511–515, doi:10.1016/0021-9290(86)90124-7.
- [36] Gerard J. Tortora, Bryan Derrickson, *Principles of Anatomy and Physiology*, John Wiley and Sons, Inc., 2009.
- [37] W. Yang, V.R. Sherman, B. Gludovatz, E. Schaible, P. Stewart, R.O. Ritchie, M.A. Meyers, On the tear resistance of skin, *Nat. Commun.* 6 (2015) 6649, doi:10.1038/ncomms7649.
- [38] V.R. Sherman, W. Yang, M.A. Meyers, The materials science of collagen, *J. Mech. Behav. Biomed. Mater.* 52 (2015) 22–50, doi:10.1016/j.jmbbm.2015.05.023.
- [39] Q. Ma, H. Cheng, K.I. Jang, H. Luan, K.C. Hwang, J.A. Rogers, Y. Huang, Y. Zhang, A nonlinear mechanics model of bio-inspired hierarchical lattice materials consisting of horseshoe microstructures, *J. Mech. Phys. Solids* 90 (2016) 179–202, doi:10.1016/j.jmps.2016.02.012.
- [40] A. Ni Annaidh, Karine Bruyere, M. Destrade, M.D. Gilchrist, C. Maurini, M. Ottenio, G. Saccomandi, Automated estimation of collagen fibre dispersion in the dermis and its contribution to the anisotropic behaviour of skin, *Ann. Biomed. Eng.* 40 (2012) 1666–1678, doi:10.1007/s10439-012-0542-3.
- [41] J.W.Y. Jor, P.M.F. Nielsen, M.P. Nash, P.J. Hunter, Modelling collagen fibre orientation in porcine skin based upon confocal laser scanning microscopy, *Ski. Res. Technol.* (2011) 149–159, doi:10.1111/j.1600-0846.2010.00471.x.
- [42] T.K. Tonge, L.M. Voo, T.D. Nguyen, Full-field bulge test for planar anisotropic tissues: Part II-A thin shell method for determining material parameters and comparison of two distributed fiber modeling approaches, *Acta Biomater* 9 (2013) 5926–5942, doi:10.1016/j.actbio.2012.11.034.
- [43] A. Buganza-Tepole, J.P. Steinberg, E. Kuhl, A.K. Gosain, Application of finite element modeling to optimize flap design with tissue expansion, *Plast. Reconstr. Surg.* 134 (2014) 785–792, doi:10.1097/PRS.0000000000000553.
- [44] Y. Lanir, Y.C. Fung, Two-dimensional mechanical properties of rabbit skin—II. Experimental results, *J. Biomech.* 7 (1974) 171–182, doi:10.1016/0021-9290(74)90058-X.
- [45] Y. Gao, A.M. Waas, J.A. Faulkner, T.Y. Kostrominova, A.S. Wineman, Micromechanical modeling of the epimysium of the skeletal muscles, *J. Biomech* 41 (2008) 1–10, doi:10.1016/j.jbiomech.2007.08.008.
- [46] J.W.Y. Jor, M.P. Nash, P.M.F. Nielsen, P.J. Hunter, Estimating material parameters of a structurally based constitutive relation for skin mechanics, *Biomech. Model. Mechanobiol* 10 (2011) 767–778, doi:10.1007/s10237-010-0272-0.
- [47] M.D. Ridge, V. Wright, The directional effects of skin, *J. Invest. Dermatol.* 46 (1965) 341–346, doi:10.1038/jid.1966.54.
- [48] M. Ottenio, D. Tran, A. Ni Annaidh, M.D. Gilchrist, K. Bruyère, Strain rate and anisotropy effects on the tensile failure characteristics of human skin, *J. Mech. Behav. Biomed. Mater.* 41 (2015) 241–250, doi:10.1016/j.jmbbm.2014.10.006.
- [49] A. Ni Annaidh, K. Bruyere, M. Destrade, M.D. Gilchrist, M. Ottenio, Characterization of the anisotropic mechanical properties of excised human skin, *J. Mech. Behav. Biomed. Mater.* 5 (2012) 139–148, doi:10.1016/j.jmbbm.2011.08.016.
- [50] Z. Liu, K. Yeung, The preconditioning and stress relaxation of skin tissue, *J. Biomed. Pharm. Eng.* 1 (2008) 22–28, doi:10.1007/s00238-011-0671-1.
- [51] M.J. Buehler, Nature designs tough collagen: explaining the nanostructure of collagen fibrils, *Proc. Natl. Acad. Sci. U. S. A.* 103 (2006) 12285–12290, doi:10.1073/pnas.0603216103.
- [52] M.J. Buehler, Nanomechanics of collagen fibrils under varying cross-link densities: atomistic and continuum studies, *J. Mech. Behav. Biomed. Mater.* 1 (2008) 59–67, doi:10.1016/j.jmbbm.2007.04.001.
- [53] Z. Qin, M.J. Buehler, Flaw tolerance of nuclear intermediate filament lamina under, *ACS Nano* 5 (2011) 3034–3042.
- [54] Z. Qin, M.J. Buehler, Impact tolerance in mussel thread networks by heterogeneous material distribution, *Nat. Commun.* 4 (2013) 2187, doi:10.1038/ncomms3187.
- [55] W. Yang, V.R. Sherman, B. Gludovatz, M. Mackey, E.A. Zimmermann, E.H. Chang, E. Schaible, Z. Qin, M.J. Buehler, R.O. Ritchie, M.A. Meyers, Protective role of arapaima gigas fish scales: structure and mechanical behavior, *Acta Biomater* 10 (2014) 3599–3614, doi:10.1016/j.actbio.2014.04.009.
- [56] S. Plimpton, Fast parallel algorithms for short-range molecular dynamics, *J. Comput. Phys.* 117 (1995) 1–19, doi:10.1006/jcph.1995.1039.
- [57] A. Stukowski, Visualization and analysis of atomistic simulation data with OVITO—the open visualization tool, *Model. Simul. Mater. Sci. Eng.* 18 (2010) 0–7, doi:10.1088/0965-0393/18/1/015012.
- [58] A. Gautieri, S. Vesentini, A. Redaelli, M.J. Buehler, Hierarchical structure and nanomechanics of collagen microfibrils from the atomistic scale up, *Nano Lett* 11 (2011) 757–766, doi:10.1021/nl103943u.
- [59] Z.L. Shen, M.R. Dodge, H. Kahn, R. Ballarín, S.J. Eppell, Stress-strain experiments on individual collagen fibrils, *Biophys. J.* 95 (2008) 3956–3963, doi:10.1529/biophysj.107.124602.
- [60] D.T. Corr, D.A. Hart, Biomechanics of scar tissue and uninjured skin, *Adv. Wound Care* 2 (2013) 37–43, doi:10.1089/wound.2011.0321.
- [61] J. Ankersen, A. E. Birkbeck, R.D. Thomson, P. Vanezis, Puncture resistance and tensile strength of skin simulants, *Proc. Inst. Mech. Eng. H* 213 (1999) 493–501, doi:10.1243/0954411991535103.
- [62] A. Mauri, R. Hopf, A.E. Ehret, C.R. Picu, E. Mazza, A discrete network model to represent the deformation behavior of human amnion, *J. Mech. Behav. Biomed. Mater.* 58 (2016) 45–56, doi:10.1016/j.jmbbm.2015.11.009.
- [63] H.C. Wells, K.H. Sizeland, N. Kirby, A. Hawley, S. Mudie, R.G. Haverkamp, Acellular dermal matrix collagen responds to strain by intermolecular spacing contraction with fibril extension and rearrangement, *J. Mech. Behav. Biomed. Mater.* 79 (2018) 1–8, doi:10.1016/j.jmbbm.2017.12.009.
- [64] S. Nesbitt, W. Scott, J. Macione, S. Kotha, Collagen fibrils in skin orient in the direction of applied uniaxial load in proportion to stress while exhibiting differential strains around hair follicles, *Materials (Basel)* 8 (2015) 1841–1857, doi:10.3390/ma8041841.
- [65] C. Flynn, A. Taberner, P. Nielsen, Mechanical characterisation of in vivo human skin using a 3D force-sensitive micro-robot and finite element analysis, *Biomech. Model. Mechanobiol* 10 (2011) 27–38, doi:10.1007/s10237-010-0216-8.
- [66] J.E. Bischoff, Reduced parameter formulation for incorporating fiber level viscoelasticity into tissue level biomechanical models, *Ann. Biomed. Eng.* 34 (2006) 1164–1172, doi:10.1007/s10439-006-9124-6.
- [67] S.E. Szczesny, D.M. Elliott, Interfibrillar shear stress is the loading mechanism of collagen fibrils in tendon, *Acta Biomater* 10 (2014) 2582–2590, doi:10.1016/j.actbio.2014.01.032.
- [68] B. Lynch, S. Bancelin, C. Bonod-Bidaud, J.B. Guesquin, F. Ruggiero, M.C. Schanne-Klein, J.M. Allain, A novel microstructural interpretation for the biomechanics of mouse skin derived from multiscale characterization, *Acta Biomater* 50 (2017) 302–311, doi:10.1016/j.actbio.2016.12.051.